Marine and Petroleum Geology 134 (2021) 105367

Contents lists available at ScienceDirect

Marine and Petroleum Geology

journal homepage: www.elsevier.com/locate/marpetgeo

Early-stage marine dolomite altered by hydrothermal fluids in the Middle Permian Maokou Formation in the eastern Sichuan Basin, Southern China

Ting Li [a,b], Dancheng Zhu [a,b], Minglei Yang [a,b], Xihua Zhang [c], Pingping Li [a,b], Chaojin Lu [a,b], Huayao Zou [a,b,*]

[a] College of Geosciences, China University of Petroleum, Beijing, Changping, Beijing, 102249, China
[b] State Key Laboratory of Petroleum Resources and Prospecting, China University of Petroleum, Beijing, Changping, Beijing, 102249, China
[c] Research Institute of Petroleum Exploration and Development, PetroChina Southwest Oil and Gas Field Company, Chengdu, 600041, China

ARTICLE INFO

Keywords:
Dolomitization
Marine dolomite
Hydrothermal fluids
Massive dolostone
Patchy dolostone
Maokou formation
Sichuan basin

ABSTRACT

Deciphering the dolomitization process is the key to understanding the formation of massive dolostones on shallow-marine platforms, it also improves our understanding of dolostone reservoirs. Hydrothermal fluids are suggested to be a potential mechanism for dolomitization; however, determining whether hydrothermal fluids are responsible for dolomitization or the recrystallization of an early dolostones is poorly understood. The dolomite of Maokou Formation (Guadalupain) in the eastern part of the Sichuan Basin is a good case study on the hydrothermal dolomitization and recrystallization. Based on petrographic observation, the massive dolostone (MD) consists of fine-crystalline dolomite (D1), fine to medium crystalline dolomite (D2) and coarse-crystalline dolomite (D3), and the patchy dolostone (PD) which is composed of medium to coarse dolomite with an euhedral to subhedral texture. Since the fine-crystalline dolomite is cross-cut by low amplitude stylolites, and is composed of euhedral dolomite with a dull red luminescence, dolomitization is interpreted to have occurred in near surface condition. While the Fe, Mn, and ∑REE concentrations, $\delta^{13}C_{VPDB}$ values, $^{87}Sr/^{86}Sr$ ratios, and REE Pattern of D1 are comparable to those of the coexisting limestone, and the $\delta^{18}O_{VPDB}$ values are slightly higher than that of the coeval limestone, indicating that the dolomitization fluid of D1 was derived from Middle Permian seawater. In contrast, zebra fabrics and saddle dolomites are common in D2 and D3, and their geochemical characteristics and cathluminescence are quite different from those of D1 but they are similar to those of the saddle dolomites. Besides, the fluid inclusions in D2 and D3 have high homogenization temperatures and salinities, which are also similar to those of the saddle dolomite. Moreover, the D2 shows an inequigranular texture, and there are no obvious boundaries between D1, D2 and D3. Therefore, the D2 and D3 were recrystallized upon D1 by hydrothermal fluids related to the Emeishan magmatism. The patchy dolostone exhibits a non-stoichiometric composition and low degree of cation ordering, suggests rapid and incomplete dolomitization. The dolomitization of PD is interpreted to be the replacement caused by hydrothermal fluids as the PD exhibits negative $\delta^{18}O_{VPDB}$ values, high homogenization temperatures and salinity, positive Eu anomalies and REE Patterns similar to those of the saddle dolomites. The porosity and stoichiometry of the D1 are higher and lower, respectively, than those of D2 and D3, and the vugs are almost entirely filled. Thus, the hydrothermal fluids were destructive for the formation of the dolostone reservoir of Maokou Formation in the study area.

1. Introduction

In general, dolomite oil and gas reservoirs have high porosity and permeability (Sun et al., 1995; Allan and Wiggins, 1993). The development of high-quality reservoirs are closely related to the degree of dolomitization. A series of dolomitization models have been proposed to interpret the ubiquitous occurrences of dolomite in stratigraphic records (Adams and Rhodes, 1960; Land, 1980; Morrow, 1982; Hardie, 1987; Tucker and Wright, 1990; Sun, 1994; Budd, 1997; Warren, 2000; Davies and Smith, 2006). However, interpreting the origin of ancient dolomite is still a challenge because the early-stage dolomite may have suffered complicated alterations (eg., recrystallization, cementation) during progressive burial (Hardie, 1987; Gregg and Shelton, 1990; Chen et al., 2004; Azomani et al., 2013). Especially, when the dolomite is influenced

* Corresponding author. College of Geosciences, China University of Petroleum, Beijing, Changping, Beijing, 102249, China.
E-mail address: huayaozou@cup.edu.cn (H. Zou).

https://doi.org/10.1016/j.marpetgeo.2021.105367
Received 16 April 2021; Received in revised form 22 September 2021; Accepted 30 September 2021
Available online 2 October 2021

by hydrothermal fluids, it is more difficult to explain the origin of the dolomite (Chen et al., 2004; Davies and Smith, 2006; Lonnee and Machel, 2006).

Hydrothermal fluids, defined as fluids with temperature and pressure higher than the temperature and pressure of the surrounding environment (White, 1957; Machel and Lonnee, 2002), are a potential source of dolomitization (John et al., 2006; Luczaj et al., 2015; Al-Ramadan et al., 2019). Hydrothermal fluids represent the geothermal anomalies, and invariably take fractures and faults as migration pathways (White, 1956; Davies et al., 2005). Hydrothermal dolomitization is

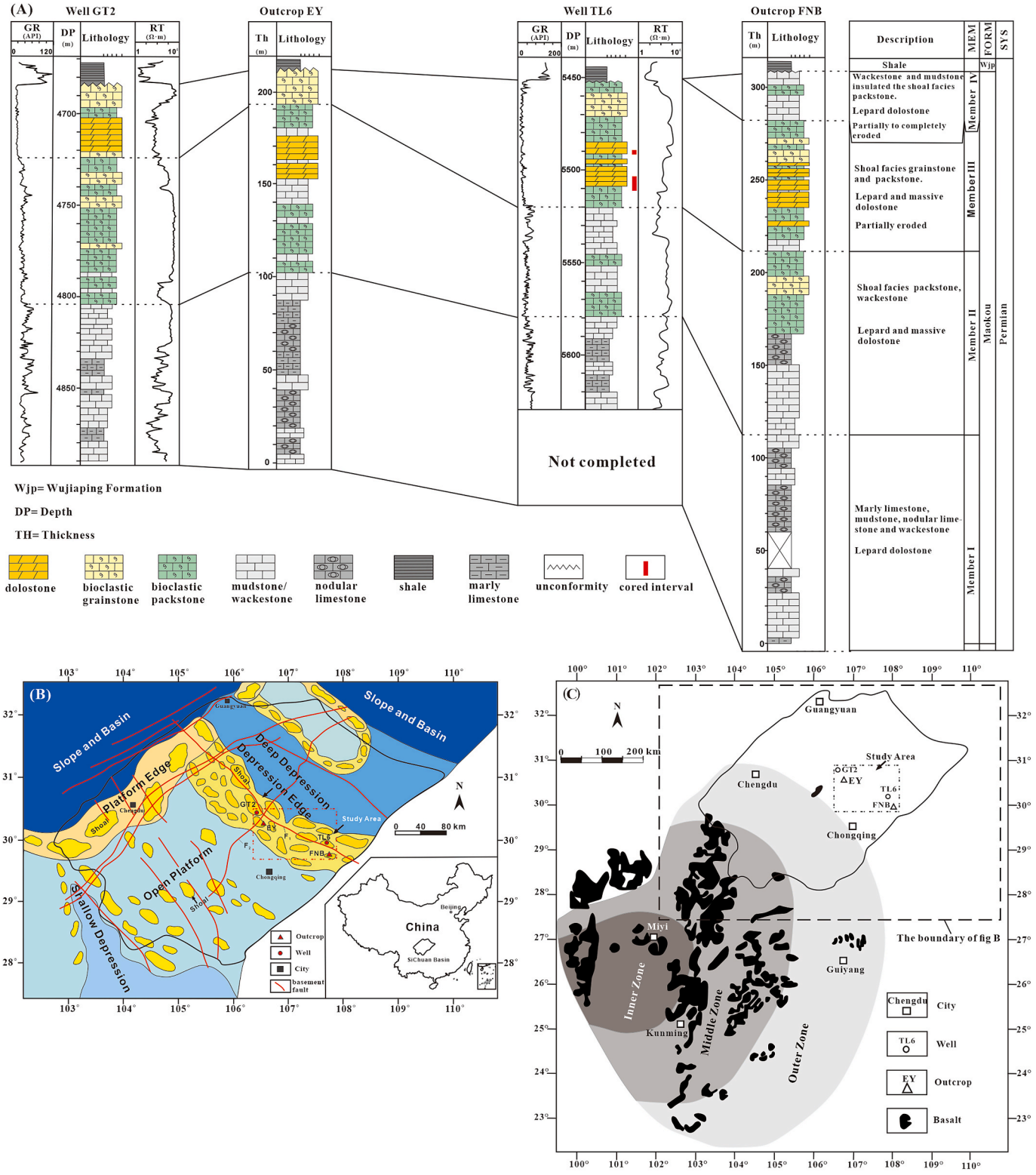

Fig. 1. **(A)** A transect showing the lithological features of the Maokou Formation. **(B)** Sedimentary facies of the second and third members of the Maokou Formation, key outcrops, and wells in the Sichuan Basin (modified from Zhou et al., 2019). **(C)** Distribution of the basalt in the Sichuan Basin, southwestern China (modified from He et al., 2003).

widespread and many dolostone reservoirs are directly related to hydrothermal fluids (John et al., 2006; Luczaj et al., 2015; Al-Ramadan et al., 2019), indicating that hydrothermal fluids may exert significant influence on the quality of the dolostone reservoirs. However, it is difficult to interpret whether the hydrothermal fluids dolomitized the limestone or modified the previously-formed dolomite. Recrystallization and chemical alteration has been demonstrated to influence matrix-replacive dolomites during hydrothermal dolomitization (Chen et al., 2004; Davies and Smith, 2006; Lonnee and Machel, 2006). It is therefore of significant importance to integrate multiple approaches of petrography, geochemistry and fluid inclusion microthermometry to constrain the origin of dolomite.

The dolostone of Maokou formation distributes in the southwestern, central, and eastern of the Sichuan Basin, with a thickness of 10–30 m (Yang et al., 2015). The dolostone in the second and third members of the Maokou Formation show a huge potential in hydrocarbon explorations (Li et al., 2013; Hu et al., 2018) (Fig. 1A). However, the origin of dolostones is debatable, which hinders the progress of gas exploration in the Maokou Formation in the Sichuan Basin. A series of dolomitization models have been proposed to explain the Maokou dolostones, including burial-replacement dolomitization (He et al., 1996; Li et al., 2020a, b), seawater dolomitization (Zhou et al., 2019), hydrothermal dolomitization (Chen at al., 2010; Jiang at al., 2014; Li et al., 2016; Jiang et al., 2017; Zhen et al., 2019) and the combination of several dolomitizing mechanisms (Wang et al., 2016; Liu et al., 2017; Li et al., 2020a, b). In fact, most of the researchers have reached the consensus that the origin of the dolomite in Maokou Formation is related to hydrothermal fluids for the following reasons: (i) The dolostone is distributed along the basement faults (Yang et al., 2015; Wang et al., 2014); (ii) Hydrothermal minerals, such as saddle dolomite, quartz and fluorite, have been identified in the dolostone in Maokou Formation (Jiang et al., 2017; Chen et al., 2012); (iii) the formation temperature of the dolomite in Maokou Formation is higher than the burial temperature (Li et al., 2020a, b; Chen et al., 2012); (iv) the geochemical characteristics, such as positive Eu anomaly, negative oxygen isotope and high $^{87}Sr/^{86}Sr$ ratios (Liu et al., 2017; Zhen et al., 2019; Li et al., 2020a, b). However, there is no conclusion as to whether the dolomite is hydrothermal in origin or hydrothermally altered (i.e., if the dolomite formed from hydrothermal fluids, or if was it modified by hydrothermal fluids). Furthermore, there are many different ideas concerning the influences of hydrothermal fluids on dolostone reservoirs (Liu et al., 2017; Hu et al., 2018; Jiang et al., 2017). Among these arguments, the biggest debate is whether the porosity can be increased by hydrothermal fluids.

Firstly, detailed petrographic work was carried out to characterize the different types of dolomite and their temporal relationships. Then, geochemical analyses of selected dolomite and calcite were implemented to evaluate the potential fluid source of the dolomitization. Fluid inclusion analyses have been conducted on some of the dolomite phases to constrain the dolomitization conditions. The purpose of this study is to determine the origin of the dolomite and the effects of hydrothermal fluids on the Maokou dolostone reservoirs.

2. Geologic setting

The study area is located in the eastern part of the Sichuan Basin. This study focuses on the outcrops Erya (EY) and Fangniuba (FNB), Well Guangtan2 (GT2) and Well Tailai6 (TL6). The Sichuan Basin, located in the southwestern part of China, is a rhombic basin that has undergone several tectonic movements, which led to periods of uplift and subsidence in the Sichuan Basin (Ma et al., 2007). Marine carbonates and shales were deposited before the Early Indosinian Movement at about 205Ma, while continental siliciclastics were deposited after the Late Indosinian Movement at about 195 Ma (Zhai, 1989).

2.1. Deposition

During the Late Carboniferous to Early Permian, the Sichuan Basin experienced uplift and erosion, causing the absence of a Lower Permian deposit in the Sichuan Basin (Ma et al., 2007). In the Middle Permain, a large-scale transgression began (Hu et al., 2012). As a result, the Sichuan Basin gradually evolved into a carbonate platform (Hu et al., 2012; Huang et al., 2017). Under this depositional setting, the Maokou Formation was deposited in the Middle Permian. The Maokou Formation (270–260 Ma, Wang and Jin, 2020) is subdivided into four members with a total thickness of 200–300 m (Fig. 1A). The Member I of Maokou Formation consists of marly limestone, nodular mudstone and mudstone, indicating a subtidal low energy environment. In contrast, bioclastic shoals dominated the deposition of the Member II and III, with bioclastic packstone and grainstone and part of these members have been dolomitized. Member IV of the Maokou Formation is composed of bioclastic wackestone. During the depositional period of the Member III of Maokou Formation, the Guangyuan-Liangping paleo-rift developed, which formed an intra-platform depression (Li et al., 2016; Zhou et al., 2019; Gao et al., 2020). Marly limestone and mudstone were deposited in the depression, indicating a deep-water sedimentary setting, while massive high-energy shoals developed at the basin margin (Fig. 1B).

2.2. Magmatism

At the end of the deposition of Maokou Formation (~260 Ma), there was an uplift caused by the Dongwu Movement which is related to the upwelling of the Emeishan Large Igneous Province (LIP). Due to the uplift, the duration of the erosion for the Maokou Formation is as long as 1–3 Ma (He et al., 2005; Xiao, 2017). At the beginning of the Late Permian (~259 Ma), the movement of Emeishan mantle plume reached its climax, and a large-scale basaltic eruption occurred in the southwestern part of the Sichuan Basin (He et al., 2003), the massive basalt partly invaded the Maokou limestone. The duration of the eruption of the Emeishan basalts is less than 3 Ma (Shellnutt et al., 2012; He et al., 2016). The center of the basaltic eruption is located in the Miyi County which is about 600 km away from the study area. The basalt in the southwestern part of the Sichuan Basin is located on the middle of the eruption zone, while most of the other parts of Sichuan Basin comprise the outer zone (Fig. 1C). The basaltic eruption caused regional thermal anomalies and and reached a peak during the Emeishan LIP at ca. 259 Ma (Zhu et al., 2010). After this, the Sichuan Basin experienced thermal

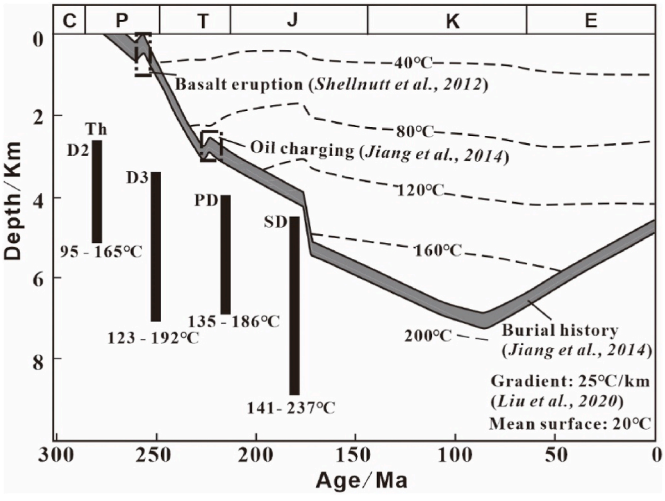

Fig. 2. Burial history of Maokou Formation in the Eastern Sichaun Basin (modified from Jiang et al., 2014). Insert dashed square indicates timing of basalt eruption and oil charging, and the black bars represent the homogenization temperatures of fluid inclusions for different types of dolomites.

subsidence, the maximum depth of burial experienced by the Maokou Formation in the eastern Sichuan Basin is approximately 7000 m (Fig. 2) (Zhu et al., 2009).

2.3. Faults

Many basement faults have developed in the Sichuan Basin, and they are divided into two groups, trending northeast and northwest, respectively (Fig. 1B). These faults, which developed before the Caledonian Orogeny, were taken shape in Himalayan Orogeny (Tong, 1992). During the late Permian, the Sichuan Basin was in an extensional system, which led to the opening of these basement faults (Tong., 1992; Tan et al., 2007). There are two faults (F1 and F2) in the study area (Fig. 1B). The Erya outcrop is close to the two faults, while the well Tailai 6 and outcrop Fangniuba are close to the fault F1 but far away (ca.100 km) from the fault F2 (Fig. 1B).

3. Samples and methods

Outcrops and wells were selected close to the basement faults in order to observe hydrothermal diagenesis. For the dolomite sample, the sampling strategy was to collect a new sample whenever a change in dolostone occurrence, dolomite crystal size, diagenetic and/or sedimentary characteristic. Where there were no major changes over 2–3 m along a section, an additional sample was taken. For the limestone sample, the sampling is focused on the limestone that suffered weak

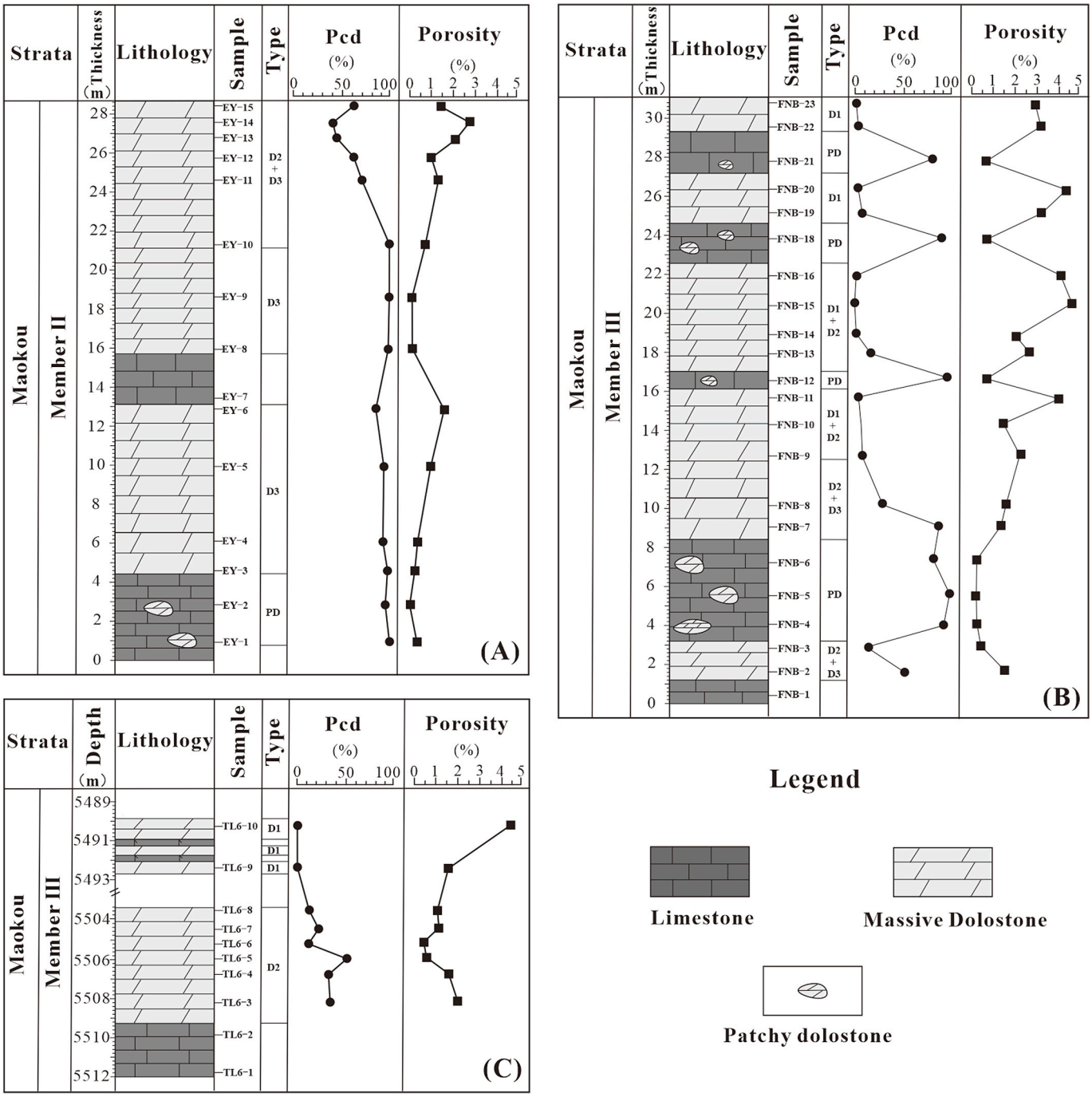

Fig. 3. Stratigraphic columns of the Maokou dolostone in (A) outcrop EY, (B) outcrop FNB, and (C) well TL6. Pcd = Percentage of coarse dolomite.

diagenetic alteration, which is to ensure that the geochemical information of the original seawater can be preserved. A total of 48 samples were collected from the FNB outcrop, EY outcrop and well TL6 at the eastern part of the Sichuan Basin (Fig. 3). The samples include dolostone, limestone and saddle dolomite that filled vugs and fractures. All the dolostone samples were classified based on their petrological characteristics, and were selected for further geochemical analysis based on the differences of petrology. The limestone samples that were selected for geochemical analysis are mudstone and bioclastic wackstone with none luminescence.

The thin sections were impregnated with blue-epoxy resin and stained with Alizarine Red, and were examined using a Nikon LV100NPOL petrographic microscope at China University of Petroleum (Beijing). Cathodoluminescence (CL) observations were carried out using the cathodoluminometer (CL8200 MK5-2) at China University of Geoscience (Wuhan), with an operating current of 250 μA at 10 kV.

The fluid inclusion microthermometry was conducted on 12 double-polished (100 μm thick) thin sections using a heating-freezing stage (THM600) at China University of Petroleum (Beijing). First, careful petrographic examination of the fluid inclusions, including their occurrences, sizes and liquid/vapor ratios, were carried out to identify whether they had primary or secondary origins (Goldstein and Reynolds, 2001). The precision of the stage was ±0.1 °C for both the homogenization temperature (T_h) and the final melting temperature (T_m). Salinity values were calculated from T_m according the equation: salinity (wt.%) = $1.78 \times T_m - 0.0442 \times (T_m)^2 + 0.000557 \times (T_m)^3$ (Bodnar, 1993).

The X-ray diffraction (XRD) analyses, Fe and Mn concentrations, rare earth elements (REE) abundances, strontium isotope ($^{87}Sr/^{86}Sr$), carbon and oxygen isotopic analyses were carried out at Beijing Research Institute of Uranium Geology. The XRD analyses were performed using a Panalytical X'pert PRO MRD System with an operating voltage of 40 kV and a current of 40 mA and the degree order of dolomite was calculated according to the method of Goldsmith and Graf (1958), and stoichiometry was determined from the position of the (104) dolomite reflection of the sample (Lumsden and Chimahusky, 1980). The analytical precision 0.02% mol. The concentrations of Fe and Mn were determined using an atomic absorption spectrometer (AAS). Powdered dolostone and limestone samples (approximately 1 g) were dissolved by 8% HCl solutions, then filtered with ashless paper and analyzed. The detection limits of Fe and Mn are 8 ppm and 5 ppm, respectively. The REE abundances were determined using an inductively coupled plasma mass spectrometer (ICP-MS). 100 mg of sample powders were digested in 1 ml 2% HNO_3 and then diluted with ultrapure H_2O to a volume about 50 ml for REE analyses. Detection limits of the REE analyses were at ppb level and the errors are less than 3%. The REE concentrations were normalized to Post-Archean Australian Shale (PAAS) (McLennan, 1989), and Ce and Eu anomalies were determined following the methods proposed by Bau and Dulski (1996).

For the carbon and oxygen isotopic analyses, 30 mg of powdered sample were reacted with anhydrous phosphoric acid at 25 °C for ~16 h for calcite and 50 °C for ~48 h for dolomite (McCrea, 2004). The analysis of the produced CO_2 gases released from the samples was conducted using a Finnigan MAT-253 mass spectrometer. All of the data are reported as per milliliter with respect to the Vienna Pee Dee Belemnite (VPDB) standard. The typical standard deviations of both the $\delta^{13}C$ and $\delta^{18}O$ isotope values are ±0.1‰.

For the strontium isotope ($^{87}Sr/^{86}Sr$) analyses, 60 mg of powdered sample were dissolved in 2.5 N HCl. Then, strontium was separated using conventional cation exchange procedures and ion exchange resin. Finally, the strontium isotope analyses were performed using a Phoenix mass spectrometer, and all of the $^{87}Sr/^{86}Sr$ values were normalized to standard NBS987, with a mean precision of less than ±0.000009.

The rock porosities and permeabilities were determined using a GDS-90F permeability tester and a QK-98 compact rock saturation device at the Petro China Southwest Oil and Gasfiled Company. The surface porosity of the thin section images was obtained using Adobe Photoshop (Zhang et al., 2009). Porosity measured from sample is the ratio of pore volume and sample volume, and porosity that measured from picture is the ratio of pore area and picture area.

4. Results

4.1. Petrography

4.1.1. Massive dolostone (MD)

The MD (Figs. 3, 4A–D), occurs as 15–25 m thick, layered dolostone and is mainly present in Member III and the upper part of Member II (Fig. 1A). It is subdivided into three crystal size classes: finely crystalline dolostone (D1), fine to middle crystalline dolostone (D2), and coarse crystalline dolostone (D3). There are no obvious boundaries between D1, D2 and D3, and the D2 and D3 were not constrained by the bedding in MD. In FNB outcrop, which is close to the fault F1, the D2 (~30%) and D3 (20%) exhibit patchy occurrence in D1 (~50%) background, and the D3 was firstly developed near the vugs, fractures and then gradually evolved to D2 spatially (Fig. 4C, H). In EY outcrop, which is close to fault F1 and fault F2, the D2 (~30%) and D3 (~70%) make up all of the MD.

(1) Finely crystalline dolomite (D1)

The D1, which is mainly developed in FNB (Fig. 3B), consists of euhedral to subhedral dolomite with a relatively unimodal crystal size distribution (50–150 μm) (Fig. 5A and B). Some bioclasts can be made out and some of the interparticle pores are preserved in D1 (Fig. 5A). In the cathodoluminescence images, D1 exhibits a dull red luminescence (Fig. 6B, E).

(2) Fine to middle crystalline dolomite (D2) and coarse crystalline dolomite (D3).

The D2 and D3 account for more than 70% by volume of the MD in the Maokou Formation. The dolomite that makes up D2 is of varying sizes (150–500 μm), and it exhibits an inequigranular texture (Fig. 5C and D). Grain-ghosts were observed in D2 (Fig. 5C and D). The D3 is a fabric destructive dolostone composed of coarse and anhedral dolomite with crystal sizes of about 500 μm (Fig. 5E and F). Both D2 and D3 are very tight, with a porosity of less than 2% (Fig. 3). Zebra fabrics, fractures, and vugs are frequently developed in D2 and D3, and most of them are cemented by saddle dolomite and calcite (Fig. 4B, C, D; 5D). In the cathodoluminescence images, the dolomites with larger amounts of D2 exhibit bright red luminescence and those with lesser amounts exhibit dark red luminescence (Fig. 6C, F), while D3 exhibits a bright red luminescence (Fig. 6G, J).

4.1.2. Patchy dolostone (PD)

The PD is patches of dolostone with length of 10–20 cm in limestone matrix (Fig. 4E and F), and developed in both of the four members of Maokou Formation and mainly distributed close to the faults and fractures. The PD may account for less than 2% by volume of limestone in the Maokou Formation. It consists of coarse and subhedral dolomite, which is characterized by a cloudy center and a clear rim (Fig. 5H). Some bioclastic remnants are also presented, and some residual pores still exist between the dolomite crystals, which have less than 1% porosity. In the cathodoluminescence images, the PD exhibits a bright red luminescence with weak luminescence zonation (Fig. 6H, K).

4.1.3. Saddle dolomite

The SD, which is only present in minor amounts, less than 1% of the total dolomite volume, exhibits wave extinction, curved crystal faces, and megacrystal size (can be > 2 mm) (Fig. 5I). This dolomite fabric fills in vugs and fracture pore spaces and is typically related to the zebra fabric (Fig. 4B, C, D, H). Under cathodoluminescence, the SD exhibits

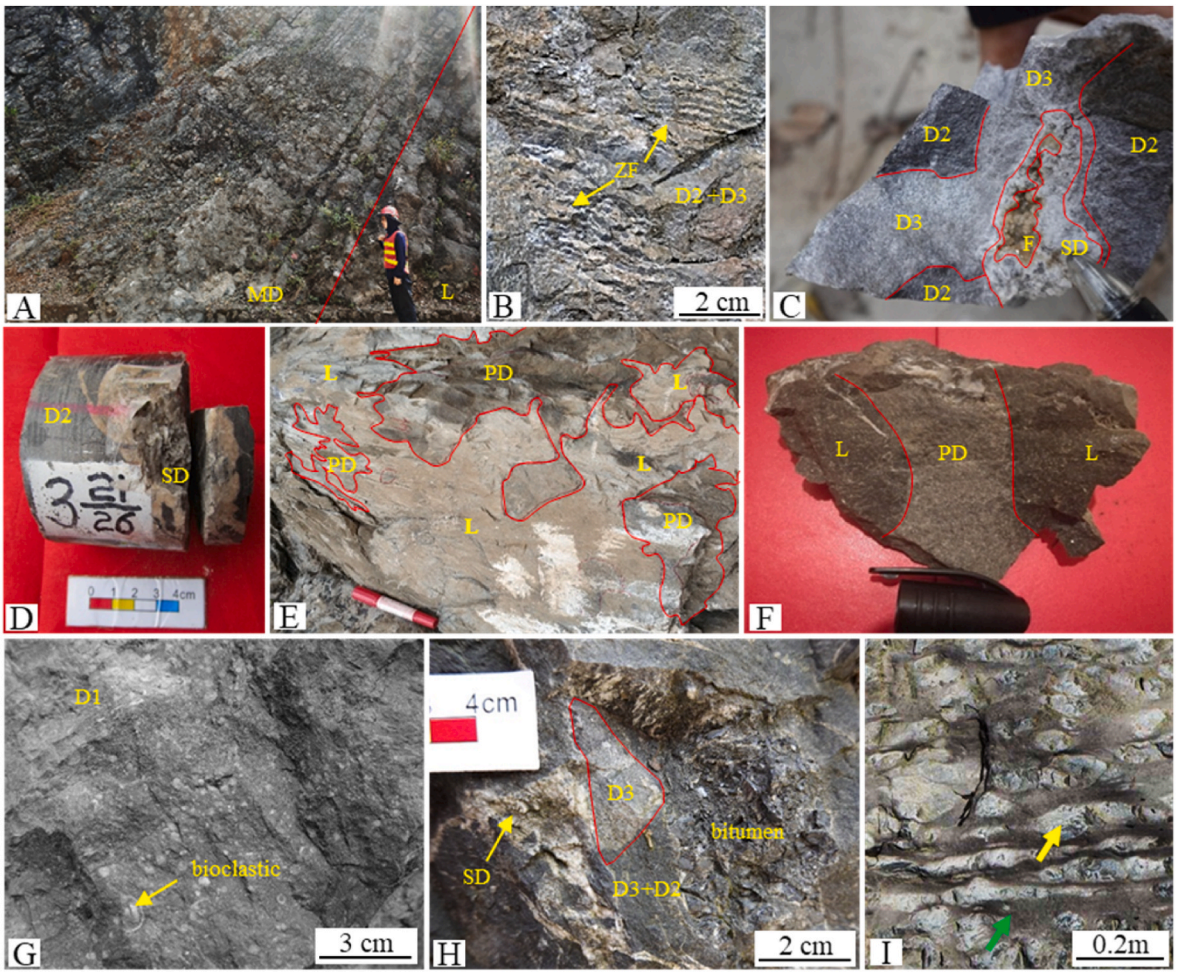

Fig. 4. Photographs showing the different lithofacies characteristics and features observed in the Maokou Formation. (A) Massive dolostone (MD) in outcrop FNB. (B) Zebra fabrics in the massive dolostone in outcrop FNB showing that the zebra fabric is cemented by dolomite and the surrounding dolostone is composed of fine to coarse dolomites (D2 + D3). (C) Hand specimen of MD from outcrop FNB showing that the vug is filled by fluorite (F) and saddle dolomite (SD) and the surrounding dolostone consists of fine to coarse dolomites (D2 + D3). (D) Core photo showing that the dissolved vugs are filled by saddle dolomite, (5505.65 m, well TL6). (E) Patchy dolostone (PD) in limestone (L) from outcrop FNB. (F) Hand specimen of the PD from outcrop FNB. (G)Some bioclastics are preserved in the fine-crystalline dolomite (D1) in outcrop FNB (H) The vugs and fractures are filled by saddle dolomite and bitumen (I) Marly limestone (green arrow) and micrite limestone (yellow arrow) from outcrop EY. (For interpretation of the references to colour in this figure legend, the reader is referred to the Web version of this article.)

weakly zoned, bright red luminescence (Fig. 6I, L).

4.1.4. Limestone

In the Maokou Formation, the host limestone can be divided into two groups: mud-dominated and grain-dominated facies. Petrographically, the mud-dominated facies are predominantly composed of mudstone and marly limestone (Fig. 4I). The grain-dominated facies are mainly composed of bioclastic grainstone and packstone with calcite cement and micrite occluding most of the pore space (Fig. 6A). The cathodoluminescence characteristic is dull to none-luminescence (Fig. 5D). The grain-dominated facies are preferentially dolomitized, while the mud-dominated facies are undolomitized (Fig. 1A).

4.1.5. Calcite cement

Calcite cement can be identified in the pores and vugs of D2 and D3 (Fig. 5F, D, J). Both of the two phases display a similar blocky texture, with crystal sizes ranging from 0.1 to 1 mm. Under cathodoluminescence, the calcite cement exhibits dull red luminescence (Fig. 6K and L)

4.1.6. Quartz and fluorite

Authigenic quartz and fluorite are observed in the vugs of D2 and D3 (Fig. 5J, K, L), and they often occur with other mineral phases (eg., calcite and saddle dolomite). Spatially, the quartz and fluorite constitute less than 1% of the mineral phases in the dolomite rocks.

4.1.7. Bitumen

The black bitumen is common in the Maokou dolostone, and usually completely fill the intercrystal pores of D1 and vugs of D2 and D3 (Fig. 5D, F, 6B).

4.1.8. Stylolite

The stylolite is characterized by the wispy and low-amplitude features in the dolomite and calcite of the Maokou Formation. The bitumen partly stains the stylolite (Fig. 7). All dolomite (D1, D2 and D3) are crosscut by the stylolite in this study.

4.2. Fe and Mn concentrations

The Fe and Mn concentrations of the limestones and dolostones are presented in Table 1. The limestone samples have Fe and Mn concentrations of 135–258.8 ppm (mean value = 186.3 ppm, SD = 52.7 ppm) and 9.8–39.3 ppm (mean value = 23.4 ppm, SD = 12.2 ppm), respectively. The Fe and Mn concentrations of D1 (183.7–382.8 ppm and

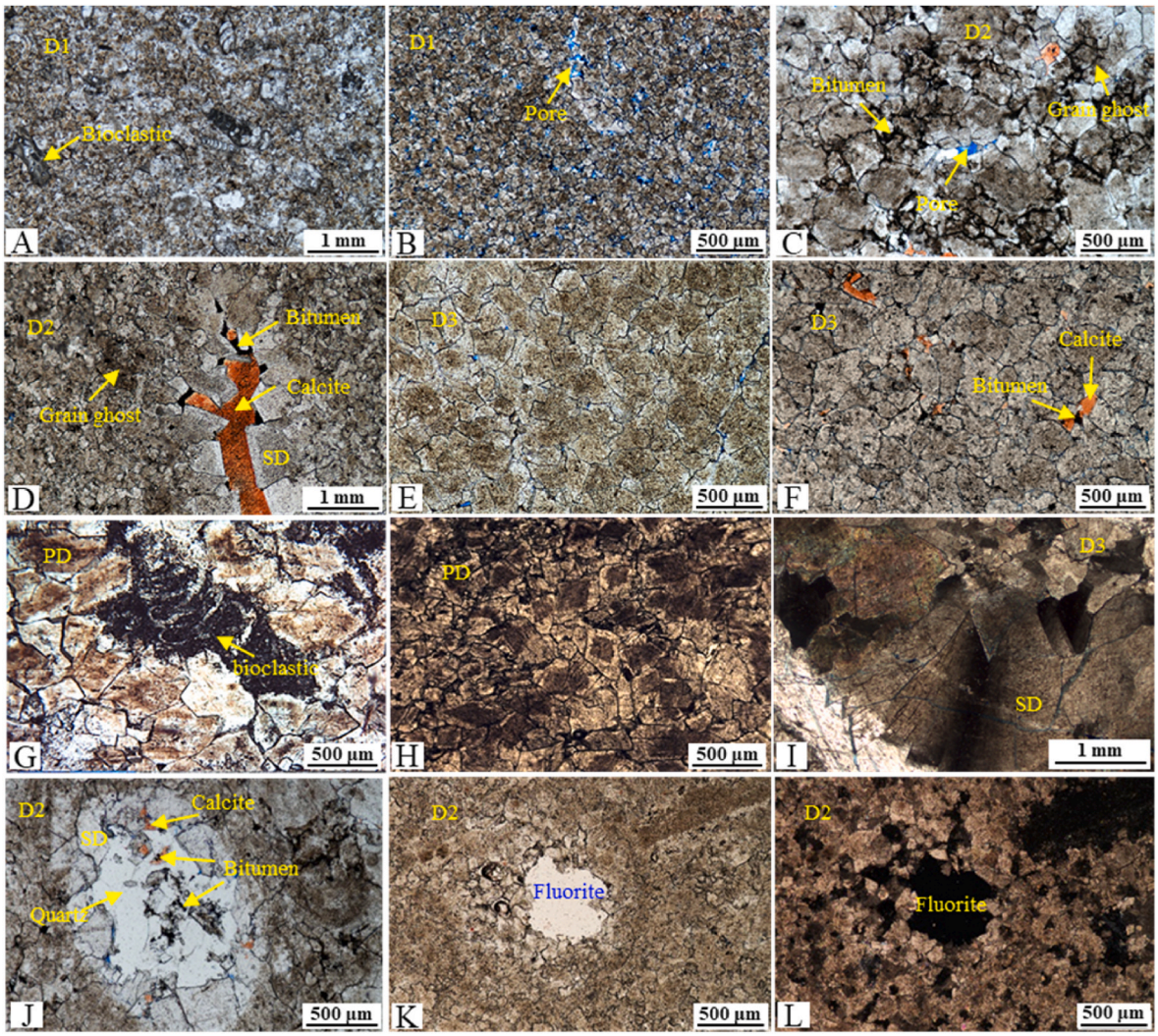

Fig. 5. Thin section photographs of the different dolostone phases of Maokou Formation. (A) D1 from outcrop FNB, the bioclastics are well preserved. (B) D1 from outcrop FNB showing fine crystals with planar-e to planar-s textures and a surface porosity about 3%. (C) D2 from outcrop EY showing a coarser crystal size than D1. The dolomites vary in size, with a surface porosity about 1%, and grain-ghosts are observed. (D) D2 from outcrop FNB, the vug is filled with saddle dolomites, calcite, and bitumen. (E) D3 from outcrop EY showing coarse and anhedral dolomite with few inter-crystal pores. (F) D3 from outcrop FNB, the inter-crystal pores are filled with calcite and bitumen. (G) PD from outcrop FNB showing coarse crystals with well-preserved bioclastics. (H) PD from outcrop EY, euhedral to subhedral dolomite with clear rims and cloudy cores. (I) A typical fracture-filling saddle dolomite with wave extinction, well TL6. (J) Image shows the filling sequence of SD, quartz, calcite and bitumen, outcrop FNB. (K, L) Same view, displaying a vug-filled fluorite with full extinction.

22–36.1 ppm, respectively), D2 (319.4–1243.8 ppm and 35.8–72.2 ppm, respectively), and D3 (861.7–1345.6 ppm and 44.8–59.6 ppm, respectively) increase in order and are higher than those of the limestone samples. More specifically, the Fe and Mn concentrations of the SD and PD are similar but are higher than those reported above. The PD has Fe and Mn concentrations of 1145.4–1971.4 ppm and 127.6–180 ppm, respectively, while those of the SD are 1006–2235.7 ppm and 99–136.2 ppm, respectively (Fig. 8A).

4.3. Mg/Ca (mol/mol) ratios and degree of cation ordering

The Mg/Ca (mol/mol) ratios and degree of cation ordering of the analyzed dolostone samples are presented in Table 1 and are plotted in Fig. 8B. The Mg/Ca (mol/mol) ratio and the degree order of D1 range from 0.79 to 0.85 (mean value = 0.83, SD = 0.02) and 0.64 to 0.72 (mean value = 0.68, SD = 0.03), respectively. D2 has Mg/Cal (mol/mol) ratios of 0.84–0.94 (mean value = 0.89, SD = 0.04) and degree orders of 0.56–0.76 (mean value = 0.64, SD = 0.07). The Mg/Cal (mol/mol) ratio of D3 ranges from 0.86 to 0.96 (mean value = 0.92, SD = 0.04), and the degree order ranges from 0.63 to 0.67 (mean value = 0.65, SD = 0.07). The PD has Mg/Ca (mol/mol) ratios of 0.68–0.81 (mean value = 0.79, SD = 0.05) and degree orders of 0.44–0.57 (mean value = 0.51, SD = 0.07).

4.4. Carbon and oxygen isotopes

The stable carbon and oxygen isotopes of the MD (D1, D2, and D3), PD, SD, and host limestone were analyzed. The data are presented in Table 1 and are plotted in Fig. 9A. The $\delta^{13}C_{VPDB}$ values of the dolostone and host limestone are similar, ranging from +2.5‰ to +4.5‰. The $\delta^{18}O_{VPDB}$ values of the dolostone are more negative than those of the limestone, except for D1. D1 has $\delta^{18}O_{VPDB}$ values of −3.3‰ to −4.9‰ (mean value = −4.0‰, SD = 0.5‰), which overlap with the $\delta^{18}O_{VPDB}$ values of the host limestone (−4.1‰ to −5.0‰, mean value = −4.6‰, SD = 0.4‰). In contrast, from D1 to D2 and D3, the $\delta^{13}C$ and $\delta^{18}O$ records exhibit a successively negative trend toward the SD member. The $\delta^{18}O_{VPDB}$ values of D2 and D3 are −6.8‰ to −7.7‰ (mean value = −7.2‰, SD = 0.4‰) and −7.2‰ to −10.3‰ (mean value = −8.8‰, SD

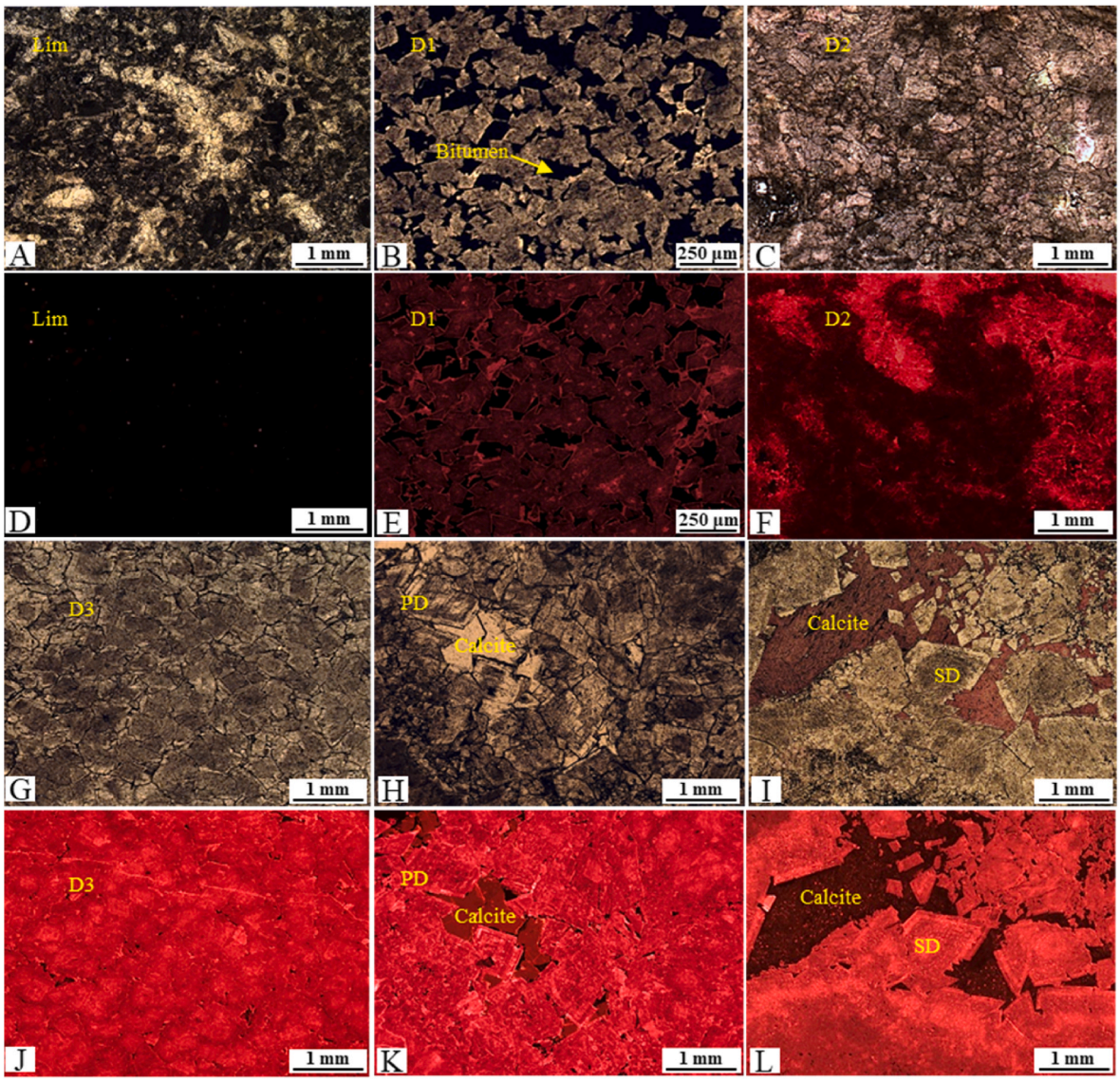

Fig. 6. Thin section photographs showing the petrographic features of samples (A–C, G–I) under plane polarized light and (D–F, J–L) cathodoluminescent light. (A, D) Same view, bioclastic limestone with non-luminescence, outcrop EY. (B, E) Same view, fine and euhedral dolomites with dull red luminescence, D1 from well TL6. (C, F) Same view, fine to coarse crystal dolomites, the larger dolomite exhibits bright red luminescence and the smaller dolomite exhibits dark red luminescence, D2 from outcrop FNB. (G, J) Same view, coarse and anhedral dolomite with bright red luminescence, D3 from outcrop EY. (H, K) Same view, euhedral to subhedral dolomite with red-zoned luminescence and calcite remnants with dull luminescence, PD from outcrop EY. (I, L) Same view, fracture-filling saddle dolomite with red-zoned luminescence and calcite remnants with dark red luminescence, outcrop FNB. (For interpretation of the references to colour in this figure legend, the reader is referred to the Web version of this article.)

= 1.2‰), respectively. The SD and PD have the narrow range of $\delta^{18}O$ values, ranging from −9.3‰ to −11.4‰ (mean value = −10.2‰, SD = 0.9‰) and −10.9‰ to −11.6‰ (mean value = −11.3%, SD = 0.3%), respectively.

4.5. $^{87}Sr/^{86}Sr$ ratios and Sr concentrations

The $^{87}Sr/^{86}Sr$ ratios of the dolostone and limestone samples are presented in Table 1. A range of $^{87}Sr/^{86}Sr$ ratios (0.7068–0.7075) has been suggested for Middle Permian seawater (Korte et al., 2006). The limestone and D1 samples yielded $^{87}Sr/^{86}Sr$ ratios of 0.707095–0.707403 (mean value = 0.707092, SD = 0.000141) and 0.707021 to 0.707823 (mean value = 0.707471, SD = 0.000286), respectively, which mostly overlap with the suggested $^{87}Sr/^{86}Sr$ ratios of Permian seawater. D2 and D3 have similar $^{87}Sr/^{86}Sr$ ratios of 0.707838–0.708725 (mean value = 0.708102, SD = 0.000284) and 0.707975 to 0.708781 (mean value = 0.708324, SD = 0.000331), relatively, which are higher than those of D1 and the limestone (Fig. 9B). The SD and PD have higher $^{87}Sr/^{86}Sr$ ratios than those reported above, ranging from 0.708236 to 0.709595 (mean value = 0.708984, SD = 0.000141) and 0.709328 to 0.710186 (mean value = 0.709757, SD = 0.000429), respectively. The Sr concentrations of the limestone samples (348.3–1177.5 ppm, mean 866.2 ppm) are the highest, followed by the PD (147.1–181.2 ppm, mean 164.1 ppm) and MD (42.3–124.7 ppm, mean 67.1 ppm), while the values of the SD (35.2–41.7 ppm, mean 38.8 ppm) are the lowest. For the MD samples, there is a negative correlation between the $^{87}Sr/^{86}Sr$ ratios and Sr concentrations (Fig. 9D).

4.6. Fluid inclusion microthermometry

The D1 lacks of vapor-liquid inclusions and the inclusions are small in size (<5 μm). Therefore, fluid inclusion microthermometry was

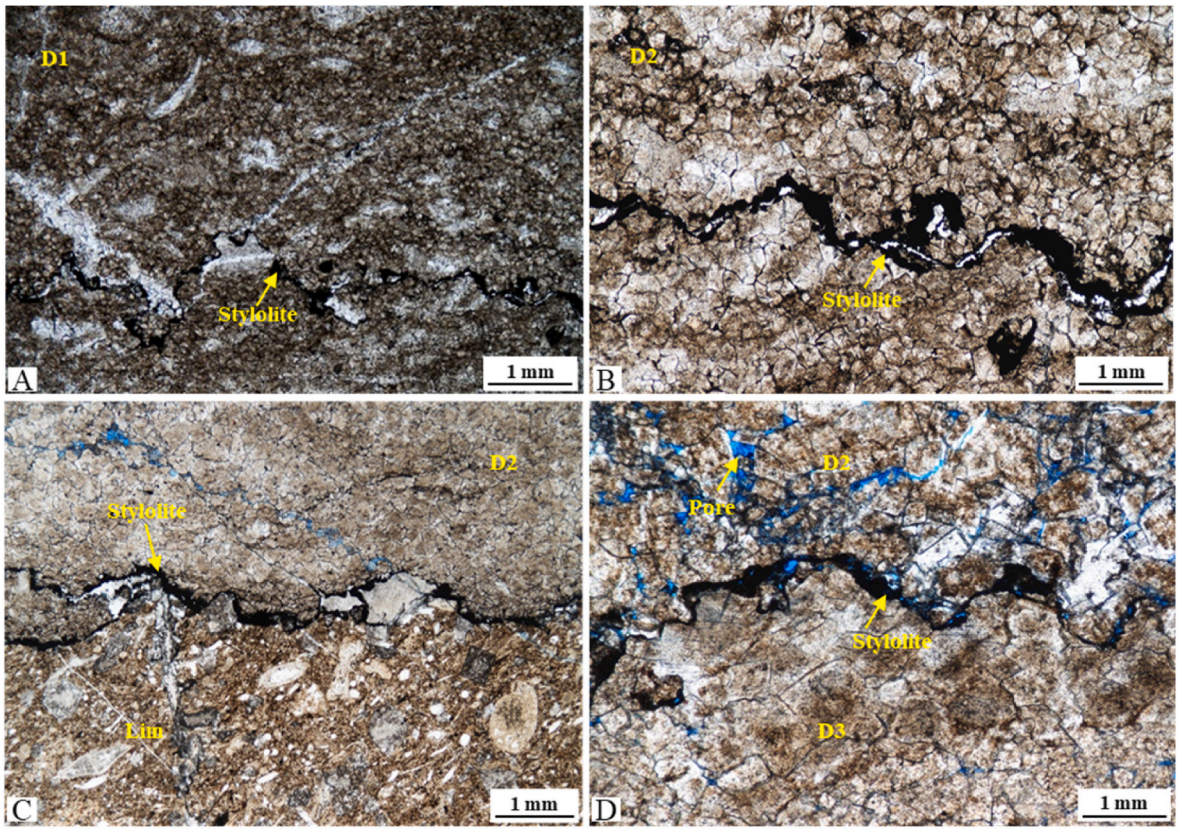

Fig. 7. Stylolite clearly postdates dolomitization of massive dolostone. No dolomite grows across stylolites and the dolomite crystals are consumed at stylolites. (A) D1 in outcrop FNB. (B) D2 in outcrop FNB. (C) the stylolite developed at the boundary of D2 and limestone, outcrop EY. (D) D2 and D3 in outcrop EY.

Table 1
The δ^{18} O, $\delta^{13}C$,$^{87}Sr/^{86}Sr$, XRD, Fe, Mn, Sr concentrations of different phases of dolomite and limestone in MaoKou Formation.

Sample ID	Type		$\delta^{18}O_{PDB}$‰	$\delta^{13}C_{PDB}$‰	$^{87}Sr/^{86}Sr$	Elemental analysis			XRD	
						Sr/ppm	Fe/ppm	Mn/ppm	Mg/Ca(mol/mol)	$DO(I_{015}/I_{110})$
FNB-23	MD	D1	−3.3	4.3	0.707701	123.2	268.1	22.0	0.85	0.64
FNB-19		D1	−4.2	4.1	0.707823	64.1	382.8	36.1	0.83	0.67
FNB-14		D1	−4.9	4.6	0.707302	116.1	183.7	28.6	/	/
TL6-9		D1	−3.9	4.2	0.707508	72.3	316.7	46.3	/	/
TL6-10		D1	−3.7	4.2	0.707021	58.6	/	/	0.79	0.72
mean value			**−4.0**	**4.3**	**0.707471**	**86.9**	**337.8**	**35.8**	**0.83**	**0.68**
FNB-13	MD	D2	−7.2	3.4	0.707935	70.1	1243.8	69.9	0.87	0.56
FNB-8		D2	−7.7	3.7	0.708725	89.7	687.9	72.2	0.84	0.63
FNB-3		D2	−6.8	3.4	0.708251	92.8	917.3	42.3	/	/
EY-13		D2	−6.8	3.8	0.707838	124.7	457.1	49.1	/	/
TL6-7		D2	−7.6	3.1	0.708167	48.6	319.4	57.7	0.94	0.61
TL6-3		D2	−6.9	3.5	0.708102	62.4	/	/	0.91	0.76
mean value			**−7.2**	**3.5**	**0.70817**	**81.4**	**725.1**	**58.2**	**0.89**	**0.64**
FNB-7	MD	D3	−8.9	2.7	0.708781	42.3	1098.2	47.8	0.93	0.67
EY-9		D3	−7.2	3.2	0.707975	44.8	861.7	59.6	0.96	0.63
EY-4		D3	−10.3	2.9	0.708324	43.5	1345.6	44.8	0.86	0.66
mean value			**−8.8**	**2.9**	**0.70836**	**43.5**	**1101.8**	**50.7**	**0.92**	**0.65**
FNB-5	PD		−10.9	4.0	0.710186	181.2	1145.4	127.6	0.76	0.44
EY-1	PD		−11.6	3.3	0.709328	147.1	1971.4	180.0	0.81	0.57
mean value			**−11.3**	**3.6**	**0.709757**	**164.1**	**1558.4**	**153.8**	**0.79**	**0.51**
FNB-9	SD		−9.3	4.2	0.709122	41.7	2235.7	99.0	/	/
EY-5	SD		−11.4	3.9	0.709595	39.6	1006.0	180.1	/	/
TL6-4	SD		−9.8	2.9	0.708236	35.2	1099.1	136.2	/	/
mean value			**−10.2**	**3.7**	**0.708984**	**38.8**	**1446.9**	**138.4**	/	/
FNB-1	Lim		−4.6	3.8	0.707384	1177.5	135.0	21.0	/	/
EY-1	Lim		−4.1	4.2	0.707095	348.3	258.8	39.3	/	/
TL6-2	Lim		−5.0	3.9	0.707403	1072.9	165.2	9.8	/	/
mean value			**−4.6**	**4.0**	**0.707294**	**866.2**	**286.3**	**23.4**	/	/

Note: XRD = X-Ray diffraction, DO = Degree of order.

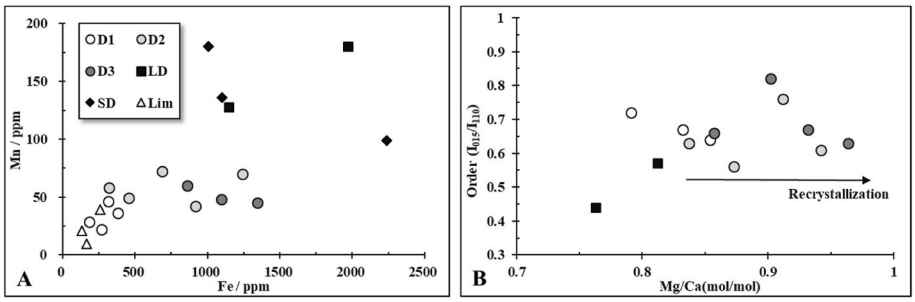

Fig. 8. **(A)** Variations in the Fe and Mn concentrations of the Middle Permian Maokou dolostone and limestone. **(B)** Mg/Ca (mol/mol) ratio vs. degree of order for the dolostone of the Middle Permian Maokou Formation in the eastern Sichuan Basin.

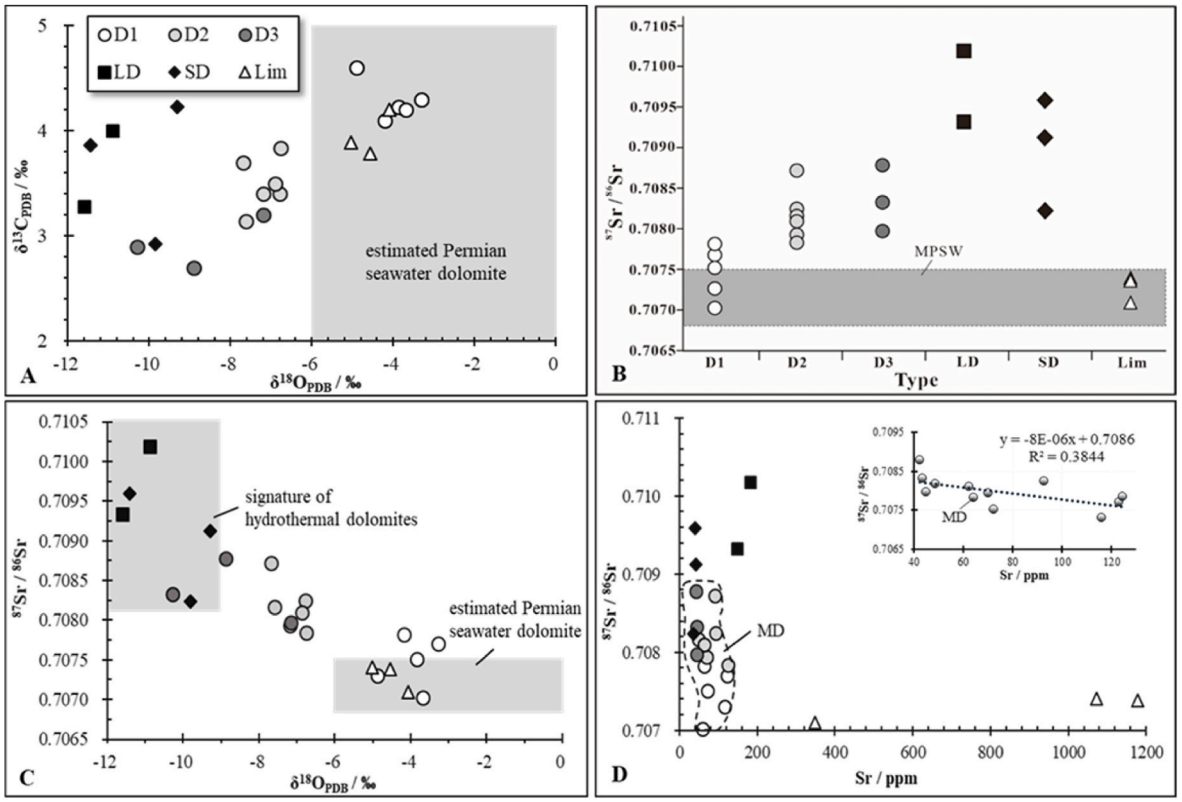

Fig. 9. (A) $\delta^{13}C$ vs. $\delta^{18}O$ for the Middle Permian Maokou dolostone and limestone in the eastern Sichuan Basin. **(B)** $^{87}Sr/^{86}Sr$ ratios of the Middle Permian Maokou dolostone and limestone from the eastern Sichuan Basin. The gray area represents the $^{87}Sr/^{86}Sr$ ratios of Middle Permian seawater (MPSW) (0.7068–0.7075; Korte et al., 2006). **(C)** Plot of $^{87}Sr/^{86}Sr$ vs. $\delta^{18}O$ of various dolomite and limestone samples. **(D)** Sr concentration vs. $^{87}Sr/^{86}Sr$ ratio for the Middle Permian Maokou dolostone and limestone in the eastern Sichuan Basin.

conducted on the D2, D3, PD, SD, and calcite cement (Cal) and the data are presented in Table 3. The primary fluid inclusions were defined following the convention of Goldstein (2012). Two phase (liquid and vapor) fluid inclusions were observed along the growth zones in the dolomite crystals and calcite cement, with the vapor accounting for 5–10% (Fig. 10A and B). Statistically, the homogenization temperatures (Th) and salinities of the samples can be grouped into: D2 (mean: 131.1 °C, 14.1 wt% NaCleq); D3 (mean: 146.6 °C, 18.6 wt% NaCleq); PD (mean: 158.1 °C, 15.1 wt% NaCleq); SD (mean: 188.1 °C, 19.3 wt% NaCleq); and Cal (mean: 135.2 °C, 14.7 wt% NaCleq) (Fig. 10C).

4.7. Rare earth elements (REE)

The concentrations of the rare earth elements in the different dolomite fabrics and the host limestone are presented in Table 2 and are plotted in Fig. 11. The total REE contents (1.39–2.44 ppm) and light rare earth elements/heavy rare earth elements (LREE/HREE) ratios (3.29–3.58) for D1 are similar to those of the host limestone (1.67–1.91 ppm; 4.01–4.31), and both have negative δEu (Lim: 0.80–0.86; D1: 0.79–0.89) and δCe (Lim: 0.28–0.47; D1: 0.42–0.47) anomalies. In contrast, the total REE concentrations and LREE/HREE ratios of D2 (3.48–4.81 ppm; 4.64–5.24), D3 (7.57–9.82 ppm; 4.40–4.50), PD (6.30–9.10 ppm; 5.93–7.04), and SD (6.94–11.71 ppm; 5.22–5.76) are higher than those of D1 and the host limestone, and these samples have positive Eu anomalies (1.1–1.5) and negative Ce anomalies (0.4–0.9) (Fig. 11D).

The Post-Archean Australian shale (PAAS; McLennan, 1989) normalized REE patterns are shown in Fig. 9A–C. The REE patterns of D1 and the host limestone exhibit a seawater-like profile (James et al., 1995) with obvious negative Ce anomalies and enriched HREEs (Fig. 11A). The REE patterns of D2 and D3 are relatively flat with positive Eu anomalies. Moreover, slightly enriched HREEs and negative Ce

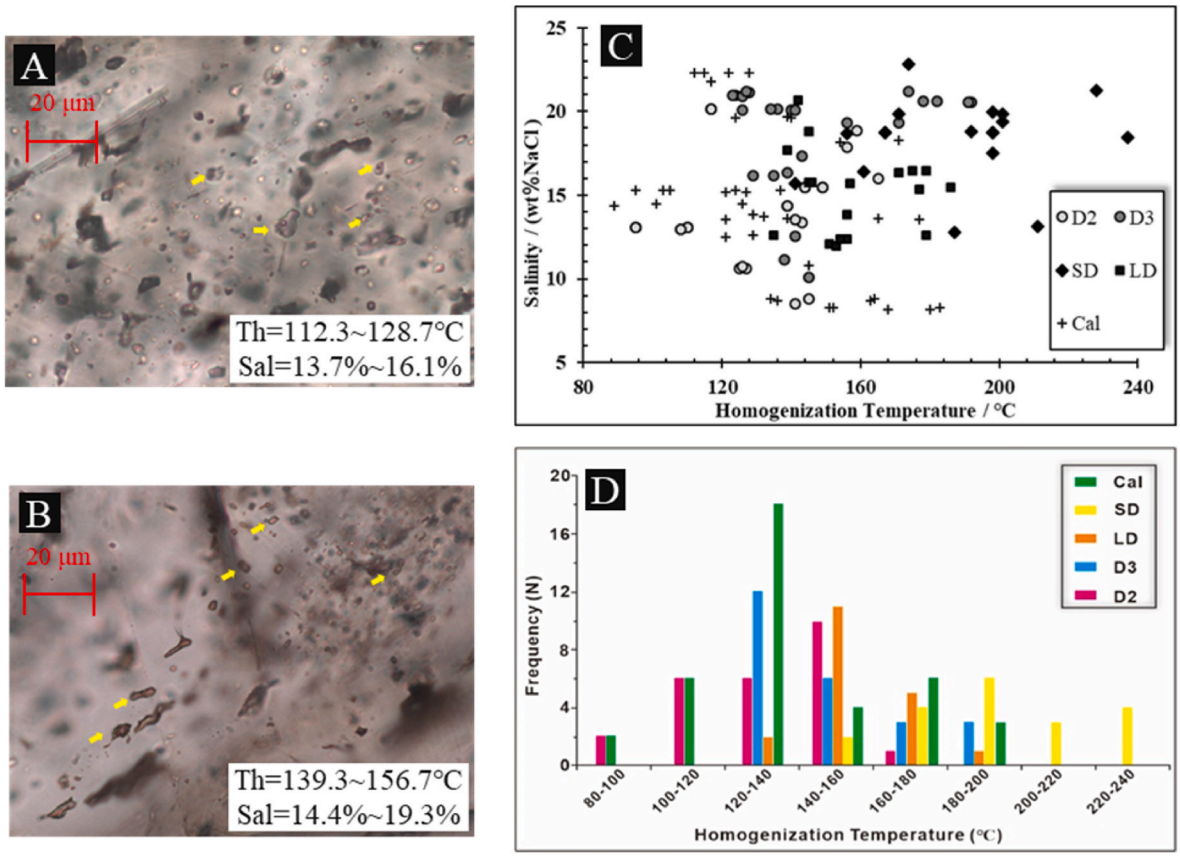

Fig. 10. Fluid inclusion study of the Maokou Formation. (A; B) Different examples of two-phase fluid inclusions in the Maokou dolomites in the eastern Sichuan Basin and their corresponding homogenization temperatures (Th) and salinities (Sal). (C) Variations in the Th and salinities of the different phases of dolomites and calcite cement. (D) Histogram of homogenization temperature of different phases of dolomites and calcite.

anomalies were also observed in the PAAS-normalized profiles of D2 and D3, which is similar to those of D1 and the limestone (Fig. 11B). The REE patterns of the PD and SD are similar to the profiles of Mid-Atlantic Ridge hydrothermal fluids (Douville et al., 2002), with obvious positive Eu anomalies and depleted HREEs (Fig. 11C).

4.8. Porosity and permeability

D1 is porous, with an average porosity of 3.4%; while the mean porosities of D2 and D3 are less than 2%. The mean surface porosity of D1 in outcrop FNB and well TL6 are 3.5% and 3.1%, respectively. In contrast, D2 (1.8% in outcrop EY, 1.9% in outcrop FNB, and 1.2% in TL6) and D3 (0.6% in outcrop EY, 1.0% in outcrop FNB) have lower mean values than D1. The PD is very tight, with a surface porosity of less than 1%. The average permeability of D1 (0.77×10^{-3} μm^2) is higher than those of D2 (0.14×10^{-3} μm^2) and D3 (0.07×10^{-3} μm^2) (Fig. 13).

5. Discussion

5.1. Paragenetic sequence

The paragenetic sequence of the Maokou dolostone is presented in Fig. 12. The crystal size of D1 is very fine to fine and shows euhedral to subhedral texture, indicating the near-surface and low-temperature formation (Gregg and Sibley, 1984). The D2 and D3 consist of coarser dolomite crystal and there are no obvious boundaries between D1, D2 and D3, it suggested that early formed D1 dolomite was followed by recrystallization and thus formed D2 and D3. As the types of D1, D2, D3 and SD were crosscut by the stylolite, it indicated that the occurrence of the stylolitization postdate the dolomitization of D1, D2 and D3 (Fig. 7). All these (D1, D2, D3, SD and stylolite) were postdated hydrocarbon migration, which occurred in the Late Triassic, as the bitumen was found filling many pores, vugs, and fractures. The bitumen stained the stylolite and the edge of the pore in D1, D2, D3 and SD. Due to the period of hydrocarbons accumulation is the late Triassic (Jiang et al., 2014), it can be assumed the development of SD is prior to the incursion of the hydrocarbon. Although there is no evidence to show the parasequence between the SD and stylolite, it can be assumed that the occurrence of the SD is earlier than the late Triassic. The Maokou Formation has been buried to 2500 m in the late Triassic (Fig. 2). In other words, this indicate the Maokou Formation is in the early-burial diagenetic stage during the period of magmatism.

The timing of formation of the vugs is equivocal. It may be that most vugs were formed before dolomitization, during a period of pre-dolomitization leaching (Zhou et al., 2019), or it may be matrix dolomite dissolution caused by burial fluids. However, no evidence of significant dolomite dissolution such as corroded rhombs lining the vugs. In some cases, the vugs appear to be enlarged fractures (Fig. 4H), indicating the burial dissolution. Therefore, the preferred interpretation is that most of the vugs were formed before dolomitization and may enlarged by subsequent burial dissolution and new vugs may be produced during burial condition.

The formation time of PD is determined according to its geochemical characteristics. The geochemical characteristics of PD are similar to those of SD and are interpreted as hydrothermal in origin (discussed below). Therefore, the formation time of PD is consistent with the time of hydrothermal activity that is resulted by the eruption of basalt.

Table 2
The abundance of rare earth elements (REE) of the Middle Permian dolostone and limestone from eastern Sichuan Basin.

Sample ID	Lith	La	Ce	Pr	Nd	Sm	Eu	Gd	Tb	Dy	Ho	Er	Tm	Yb	Lu	∑REE	∑LREE	∑HREE	δEu	δCe
FNB-1	Lim	0.689	0.576	0.111	0.487	0.096	0.020	0.123	0.020	0.128	0.028	0.081	0.010	0.060	0.008	2.438	1.979	0.459	0.856	0.473
TL6-2	Lim	0.489	0.227	0.069	0.265	0.052	0.010	0.066	0.011	0.074	0.018	0.052	0.007	0.044	0.006	1.389	1.112	0.277	0.803	0.276
FNB-23	D1	0.548	0.441	0.083	0.308	0.072	0.014	0.092	0.016	0.112	0.030	0.089	0.012	0.082	0.012	1.914	1.468	0.447	0.794	0.466
TL6-9	D1	0.462	0.394	0.101	0.275	0.058	0.013	0.076	0.013	0.098	0.023	0.071	0.011	0.062	0.009	1.666	1.302	0.364	0.886	0.421
TL6-7	D2	0.810	0.601	0.110	0.449	0.087	0.027	0.112	0.017	0.104	0.025	0.071	0.008	0.052	0.008	2.482	2.084	0.398	1.235	0.448
EY-13	D2	1.267	1.142	0.236	1.056	0.214	0.042	0.235	0.043	0.275	0.051	0.125	0.014	0.096	0.015	4.812	3.958	0.854	0.882	0.479
EY-9	D3	2.062	1.970	0.362	1.387	0.335	0.077	0.327	0.067	0.448	0.083	0.224	0.027	0.175	0.026	7.570	6.193	1.377	1.099	0.521
EY-4	D3	3.042	2.048	0.448	1.931	0.415	0.112	0.422	0.087	0.544	0.117	0.330	0.043	0.243	0.035	9.818	7.996	1.821	1.257	0.395
FNB-5	LD	2.200	3.074	0.397	1.584	0.402	0.128	0.457	0.072	0.402	0.066	0.149	0.020	0.132	0.015	9.098	7.784	1.313	1.392	0.753
EY-1	LD	1.925	1.770	0.293	1.236	0.227	0.063	0.253	0.042	0.231	0.043	0.096	0.013	0.092	0.013	6.299	5.515	0.784	1.232	0.532
FNB-9	SD	2.661	4.413	0.462	1.844	0.433	0.164	0.608	0.088	0.468	0.087	0.280	0.032	0.148	0.021	11.709	9.978	1.732	1.457	0.909
TL6-2	SD	1.685	2.355	0.310	1.124	0.264	0.083	0.312	0.050	0.291	0.062	0.174	0.025	0.175	0.026	6.937	5.822	1.115	1.336	0.747

Note: Lith = Lithology, $\sum$LREE = La + Ce + Sm + Eu, $\sum$LREE = Gd + Tb + Dy + Ho + Er + Yb + Lu, $\delta Eu = 2Eu_{SN}/(Sm_{SN} + Gd_{SN})$, $\delta Ce = 2Ce_{SN}/(La_{SN} + Pr_{SN})$, The "SN" denotes PAAS-normalized values.

5.2. Timing of dolomitization of massive dolostone

The formation depth and burial temperature of the dolostone can be constrained based on the paragenetic cross-cutting relationships and the application of the current geothermal gradient to the depths associated with stylolite formation. The aforementioned study suggests that the development of the dolomitization is earlier than the accumulation of hydrocarbon which occurred at the late Triassic period (Jiang et al., 2014) (Fig. 2). The burial depth of Maokou Formation is about 2500 m in late Triassic. If the formation thermal gradient is no more than 30–40 °C/km, the burial temperature at the late Triassic is no more than 100 °C. Besides, low-amplitude stylolite frequently crosscut the MD and are mudded by organic material (e.g., bitumen) (Fig. 7). The fact that the low amplitude stylolite crosscut the dolomite indicates that the dolomitization predated the stylolitization. The formation of stylolite in carbonate rocks may start at burial depths of 500 m to 1 km (Machel, 2004; Beaudoin et al., 2016), suggesting that this dolomitization occurred at depths of less than 1 km, although the possibility of greater depths for the onset of stylolitization cannot be ruled out. Overall, the timing of dolomitization is in the shallow-buried diagenetic stage which is buried no more than 2500 m corresponding to about 80–100 °C in formation temperature.

5.3. Origin of the dolomite

There are various types of dolostone in Maokou Formation, including MD (D1, D2, and D3), PD, and SD, and they have different spatial distribution and textures. The occurrences and crystal textures of the dolomites contain genetic information and can be used to explain the formation condition of the dolomite (Sibley et al., 1987; Warren, 2000; Jones et al., 2005; Huang et al., 2014). In general, dolomitization in near-surface environments tends to preserve the texture of the original limestone, while burial dolomitization often forms fabric-destructive dolostone (Machel, 2004). Both of these two types were observed in Maokou formation (Fig. 5), indicating that the origin and evolution of the Maokou dolostones is complicated. This hypothesis is supported by the diversiform luminescence (Fig. 6). The combined petrography, spatial distribution, and geochemical data suggest the following interpretations.

5.3.1. Saddle dolomite (SD)

The SD commonly filled the fractures and vugs of MD, suggesting that their formation was related to fracturing and/or tectonic events. The quartz and fluorite, which are considered to be a hydrothermal assemblage (Davies and Smith, 2006), are associated with the occurrence of the SD (Figs. 4B and 5J, K, L). Although saddle dolomite is a key indicator of hydrothermal setting, it is not a necessary diagnostic of hydrothermal fluids (Qing et al., 1994; Davies and Smith., 2006). According to White (1957), the temperature of hydrothermal fluids was at least 5–10 °C higher than that of ambient. The aforementioned study suggest the development of the SD should be earlier than the intrusion of bitumen that corresponds to the accumulation of the hydrocarbon at the late Triassic. Correspondingly, the burial temperature during the development of SD is no higher than 100 °C (Jiang et al., 2014). The homogeneous temperature of fluid inclusion in SD range from 141.6 to 237.3 °C indicate the alternation from hydrothermal pulse.

5.3.2. Massive dolostone (D1)

The majority of D1consist of finely to very finely crystalline dolomite (10–100 μm), with a euhedral to subhedral texture (Fig. 5A and B), which are interpreted to have resulted from penecontemporaneous to near-surface dolomitization at relatively low temperatures (Gregg et al., 1984; Sibley et al., 1987; Qing et al., 1998; Guo et al., 2016; Zheng et al., 2019). The absence of two-phase fluid inclusions further confirms that D1 was formed at low temperatures (Machel, 2004). Moreover, the Fe (mean: 337.8 ppm) and Mn (mean: 35.8 ppm) concentrations of D1 are

Table 3
Fluid inclusion data of different phases of dolomite and calcite cements of Maoku Formation in eastern Sichuan Basin.

Sample ID	Mineral type	occurrences	Th/ °C	Tm-ice/ °C	Salinity(wt.% NaCl)	Sample ID	Mineral type	occurrences	Th/ °C	Tm-ice/ °C	Salinity (wt.% NaCl)
FNB-3	D2-dolomite	cluster	145.5	−5.5	8.5	EY-4	D3-dolomite	cluster	182.4	−17.1	20.6
FNB-3	D2-dolomite	cluster	139.3	−10.4	14.4	EY-4	D3-dolomite	cluster	192.4	−17.1	20.52
FNB-3	D2-dolomite	cluster	141.7	−5.5	8.5	EY-4	D3-dolomite	cluster	191.6	−17.1	20.52
FNB-3	D2-dolomite	cluster	159.3	−15.2	18.8	EY-4	D3-dolomite	cluster	174.4	−18.8	21.19
FNB-3	D2-dolomite	cluster	156.2	−14.1	17.9	EY-4	D3-dolomite	cluster	178.4	−17.1	20.6
FNB-3	D2-dolomite	cluster	165.6	−12	16.0	EY-4	D3-dolomite	cluster	1563	−15.8	19.29
FNB-3	D2-dolomite	cluster	127.3	−7.1	10.6	EY-4	D3-dolomite	cluster	171.2	−15.8	19.29
FNB-3	D2-dolomite	cluster	125.5	−7.1	10.6	FNB-7	D3-dolomite	cluster	124.8	−18	20.96
FNB-3	D2-dolomite	cluster	126.3	−7.2	10.7	FNB-7	D3-dolomite	cluster	126.8	−18.1	20.89
TL6-5	D2-dolomite	cluster	110.7	−9.2	13.1	FNB-7	D3-dolomite	cluster	123.9	−18.1	20.96
TL6-5	D2-dolomite	cluster	95.9	−9.2	13.1	FNB-7	D3-dolomite	cluster	128.7	−18.5	21.11
TL6-5	D2-dolomite	cluster	108.3	−9.1	13.0	FNB-7	D3-dolomite	cluster	127.7	−18.5	21.19
TL6-5	D2-dolomite	cluster	144.4	−11.5	15.5	FNB-7	D3-dolomite	cluster	143.2	−13.8	17.35
TL6-5	D2-dolomite	cluster	149.2	−11.5	15.5	FNB-7	D3-dolomite	cluster	139.5	−12.6	16.35
TL6-5	D2-dolomite	cluster	117.3	−17.1	20.3	EY-9	D3-dolomite	cluster	141.3	−8.8	12.53
TL6-5	D2-dolomite	cluster	110.8	−9.2	13.1	EY-9	D3-dolomite	cluster	138.2	−7.5	11.15
TL6-5	D2-dolomite	cluster	95.9	−9.2	13.1	EY-9	D3-dolomite	cluster	145.7	−7.1	10.07
TL6-5	D2-dolomite	cluster	108.4	−9.1	13.0	EY-9	D3-dolomite	cluster	126.8	−16.8	20.07
TL6-5	D2-dolomite	cluster	144.4	−11.5	15.5	EY-9	D3-dolomite	cluster	136.7	−16.9	20.15
FNB-8	D2-dolomite	cluster	149.6	−11.5	15.5	EY-9	D3-dolomite	cluster	134.7	−16.9	20.15
FNB-8	D2-dolomite	cluster	117.3	−16.8	20.1	EY-9	D3-dolomite	cluster	140.2	−16.8	20.07
FNB-8	D2-dolomite	cluster	143.6	−9.5	13.4	EY-9	D3-dolomite	cluster	141.6	−16.8	20.07
FNB-8	D2-dolomite	cluster	139.8	−10.2	14.1	EY-9	D3-dolomite	cluster	135.3	−12.3	16.16
FNB-8	D2-dolomite	cluster	141.4	−9.6	13.5	EY-9	D3-dolomite	cluster	129.4	−12.3	16.15
TL6-5	vug-filled calcite	cluster	130.7	−5.2	8.1	FNB-5	LD-dolomite	cluster	145.4	−15.1	18.81
TL6-5	vug-filled calcite	cluster	95.9	−11.3	15.3	FNB-5	LD-dolomite	cluster	139.2	−14.1	17.68
TL6-5	vug-filled calcite	cluster	127.4	−11.2	15.2	FNB-5	LD-dolomite	cluster	135.3	−8.8	12.6
TL6-5	vug-filled calcite	cluster	105.4	−11.3	15.3	FNB-5	LD-dolomite	cluster	142.3	−17.5	20.68
TL6-5	vug-filled calcite	cluster	154.8	−14.4	18.1	FNB-5	LD-dolomite	cluster	156.4	−9.9	13.8
TL6-5	vug-filled calcite	cluster	121.1	−8.8	12.6	FNB-5	LD-dolomite	cluster	175.4	−12.5	16.45
TL6-5	vug-filled calcite	cluster	129.1	−8.9	12.7	FNB-5	LD-dolomite	cluster	179.7	−12.5	16.45
TL6-5	vug-filled calcite	cluster	126.2	−10.5	14.5	FNB-5	LD-dolomite	cluster	151.7	−8.3	12.05
TL6-5	vug-filled calcite	cluster	101.8	−10.5	14.5	FNB-5	LD-dolomite	cluster	153.8	−8.7	11.93
TL6-5	vug-filled calcite	cluster	89.7	−10.4	14.4	FNB-5	LD-dolomite	cluster	177.8	−10.8	15.37
FNB-8	vug-filled calcite	cluster	137.8	−11.3	15.3	FNB-5	LD-dolomite	cluster	186.8	−11.3	15.47
FNB-8	vug-filled calcite	cluster	103.6	−11.3	15.3	FNB-5	LD-dolomite	cluster	156.5	−11.2	12.39

(*continued on next page*)

Table 3 (*continued*)

Sample ID	Mineral type	occurrences	Th/ °C	Tm-ice/ °C	Salinity(wt.% NaCl)	Sample ID	Mineral type	occurrences	Th/ °C	Tm-ice/ °C	Salinity (wt.% NaCl)
FNB-8	vug-filled calcite	cluster	121.6	−11.2	15.2	EY-1	LD-dolomite	cluster	154.2	−11.2	12.39
FNB-8	vug-filled calcite	cluster	124.4	−11.3	15.3	EY-1	LD-dolomite	cluster	171.3	−12.4	16.34
EY-4	vug-filled calcite	cluster	171.5	−14.9	18.6	EY-1	LD-dolomite	cluster	179.2	−8.8	12.62
EY-4	vug-filled calcite	cluster	145.6	−7.3	10.9	EY-1	LD-dolomite	cluster	145.1	−11.8	15.76
EY-4	vug-filled calcite	cluster	139.4	−16.3	19.7	EY-1	LD-dolomite	cluster	157.7	−11.8	15.67
EY-4	vug-filled calcite	cluster	124.7	−16.2	19.6	EY-1	LD-dolomite	cluster	146.6	−11.8	15.76
EY-4	vug-filled calcite	cluster	140.7	−16.2	19.6	EY-1	LD-dolomite	cluster	158.5	−11.1	15.1
EY-4	vug-filled calcite	cluster	117.3	−19.1	21.8	TL6-5	vug-filled SD	cluster	198.5	−15.1	18.72
EY-4	vug-filled calcite	cluster	128.7	−19.9	22.3	TL6-5	vug-filled SD	cluster	167.4	−15.1	18.72
EY-4	vug-filled calcite	cluster	112.4	−19.9	22.3	TL6-5	vug-filled SD	cluster	192.5	−15.2	18.8
EY-4	vug-filled calcite	cluster	122.2	−19.9	22.3	TL6-5	vug-filled SD	cluster	171.5	−16.5	19.86
EY-4	vug-filled calcite	cluster	115.3	−10	13.9	TL6-5	vug-filled SD	cluster	201.5	−16.5	19.86
FNB-7	pore-filled calcite	cluster	134.1	−5.7	8.8	TL6-5	vug-filled SD	cluster	198.3	−16.7	19.98
FNB-7	pore-filled calcite	cluster	136.7	−5.6	8.7	TL6-5	vug-filled SD	cluster	211.2	−9.3	13.11
FNB-7	pore-filled calcite	cluster	164.4	−5.7	8.8	TL6-7	vug-filled SD	cluster	228.2	−18.4	21.22
FNB-7	pore-filled calcite	cluster	163.4	−5.6	8.7	TL6-7	vug-filled SD	cluster	237.3	−14.8	18.43
FNB-7	pore-filled calcite	cluster	165.8	−9.8	13.7	TL6-7	vug-filled SD	cluster	198.7	−13.8	17.5
FNB-7	pore-filled calcite	cluster	121.6	−9.6	13.5	TL6-7	vug-filled SD	cluster	198.7	−15.1	18.72
FNB-7	pore-filled calcite	cluster	139.3	−9.7	13.6	TL6-7	vug-filled SD	cluster	167.4	−15.1	18.72
FNB-7	pore-filled calcite	cluster	177.4	−9.6	13.5	TL6-7	vug-filled SD	cluster	187.4	−8.9	12.8
FNB-7	pore-filled calcite	cluster	129.7	−9.9	13.8	TL6-7	vug-filled SD	cluster	141.6	−11.8	15.7
FNB-7	pore-filled calcite	cluster	132.4	−9.8	13.7	EY-4	vug-filled SD	cluster	201.3	−16.9	19.4
EY-9	pore-filled calcite	cluster	151.4	−5.3	8.3	EY-4	vug-filled SD	cluster	174.3	−20.8	22.8
EY-9	pore-filled calcite	cluster	168.7	−5.2	8.1	EY-4	vug-filled SD	cluster	156.7	−13.9	18.7
EY-9	pore-filled calcite	cluster	152.8	−5.3	8.3	EY-4	vug-filled SD	cluster	161.5	−12.4	16.4
EY-9	pore-filled calcite	cluster	183.5	−5.3	8.3	EY-4	vug-filled SD	cluster	188.4	−15.8	19.3

close to the values of the host limestone (Fe: 286.3 ppm, Mn: 23.4 ppm) (Fig. 8A), and under CL, D1 exhibits no or dull red cathodoluminescence (Fig. 6B, E), which also supports the hypothesis that D1 was to the result of penecontemporaneous to near-surface dolomitization.

As was discussed above, the δ^{13} C values (+4.1‰ to + 4.6‰ VPDB) of D1 are quite similar to those of the host limestone (+3.8‰ to + 4.2‰ VPDB) and they fall within the estimated δ^{13}C range (0‰ to + 6‰ VPDB) (Veizer et al., 1999) of calcite precipitated from Permian seawater (Fig. 9A), implying that D1 was formed by dolomitizing fluids related to Permian seawater (Land, 1980; Banner and Hanson, 1990; Tucker and Wright, 1990; Budd, 1997). Theoretically, because of the fractionation of oxygen isotopes, the δ^{18}O values of seawater dolomite should be 1–3‰ higher than the δ^{18}O values of limestone deposited in the same seawater (Land, 1980; Vahrenkamp, 1990). The δ^{18}O values (−3.3‰ to −4.9‰ VPDB) of D1 are slightly higher than those of the host limestone (−4.1‰ to −5.0‰ VPDB) (Fig. 9A), which also supports the hypothesis that the dolomitization fluids that formed D1 were related to Permian seawater. The fluid conditions responsible for the formation of D1 are also supported by the $^{87}Sr/^{86}Sr$ ratios (0.707021–0.70823), which are largely overlap with those of the host limestone (0.707095–0.707403) and the estimated $^{87}Sr/^{86}Sr$ range of the coeval seawater (0.7068–0.7075) (Korte et al., 2006) (Fig. 9B). However, the slightly radiogenic Sr isotope signatures of D1 may be the result of enhanced fluid-rock interactions at higher temperatures as the host rock was progressively buried deeper (Montañez, 1994; Banner, 1995; Chen et al., 2004; Guo et al., 2016), which is also supported by the slightly bright cathodoluminescence around the pores of D1 (Fig. 6E). In addition, the total REE concentrations of D1 (1.7–1.9 ppm) are similar to those of the host limestone (1.4–2.4 ppm), and both of them exhibit obvious negative Ce anomalies (Fig. 11D). Moreover, the PAAS normalized REE patterns of D1 are HREE enriched (Fig. 11A) and are similar to the REE patterns of the host limestone and seawater (James et al., 1995). In summary, D1 was formed in the dolomitizing fluids related to coeval seawater under penecontemporaneous to near-surface

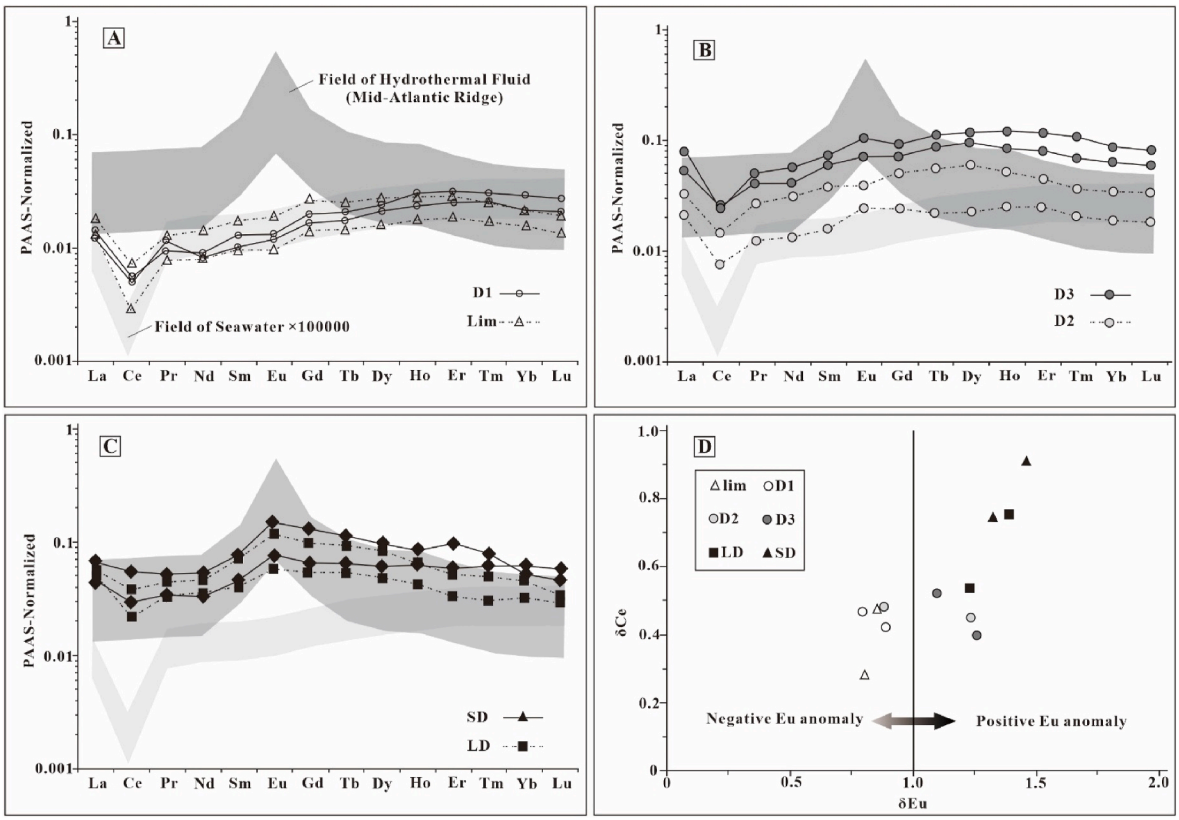

Fig. 11. PAAS-normalized patterns of (A) limestone and D1, (B) D2 and D3, (C) PD and SD, and (D) the variation in δCe and δEu in the Middle Permian Maokou Formation in the eastern Sichuan Basin. The seawater REE profile is from Alibo and Nozaki (1999), while the hydrothermal fluid profiles are from Douville et al. (2002).

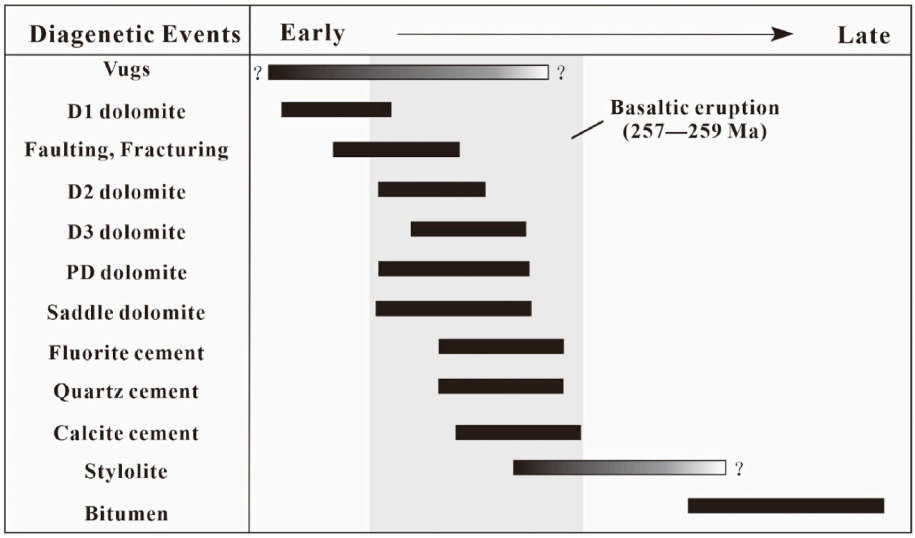

Fig. 12. Paragenetic sequence in dolostone from Maokou Formation in the eastern Sichuan Basin. The gray area represents the age of basaltic eruption (257–259 Ma; Shellnutt et al., 2012).

conditions.

5.3.3. Massive dolostone (D2 and D3)

The absence of obvious boundaries between D1, D2, and D3 suggests that the massive dolostone experienced recrystallization after formation. The mean Mg/Ca (mol/mol) ratios of D1 (0.82), D2 (0.89) and D3 (0.92) display an increasing trend, which also support the recrystallization. The D2 and D3 were likely recrystallized by the fluids responsible for the saddle dolomite based on their close spatial association and the transitional contact between them along the margin of the vugs and fractures (Fig. 4C, H). In contrast to D1, D2 and D3 dolomite is coarser, more curved (anhedral), and tightly-packed (Fig. 5C–F), indicating alteration at higher temperatures (Gregg and Sibley, 1984; Gregg and Shelton, 1990; Montañez, 1994; Qing and Mountjoy, 1994; Al-Aasm, 2003), which is probably related to high-temperature fluids during the subsequent burial diagenesis and/or hydrothermal fluids. The coarser

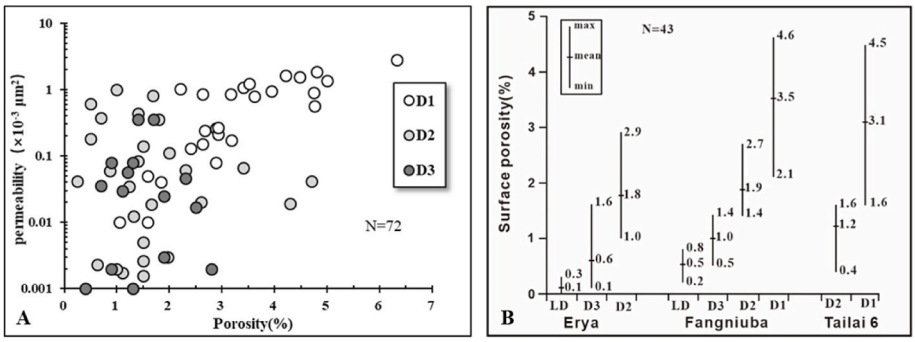

Fig. 13. (A) Plots of porosity versus permeability of Maokou dolostone in study area and (B) surface porosity of Maokou dolostone in outcrop EY, FNB and well TL6.

dolomites in D2 and D3 suggested to have resulted from recrystallization and subsequent coalescence of increased crystals based on the inequigranular texture (Fig. 5C) and CL pattern of D2 (Fig. 6C, F). Furthermore, the zebra fabrics in D2 and D3 imply alteration by hydrothermal fluids.

This interpretation is also supported by the geochemical characteristics and fluid inclusion homogenization temperature of D2 and D3. First, D2 and D3 have $\delta^{18}O$ values and $\delta^{13}C$ values lower than those of D1 and dolomite precipitated from Middle Permian seawater (Fig. 9), suggesting that D2 and D3 may experience a higher temperature than D1. Furthermore, The MD was formed before Late Triassic when the burial temperature of Maokou Formation was about 100 °C. However, the mean Th of D2 and D3 is 30–40 °C higher than the burial temperature (Fig. 2), suggesting that the D2 and D3 were altered by hydrothermal fluids. Further, the Fe and Mn concentrations and $^{87}Sr/^{86}Sr$ ratios of D2 and D3 are higher than those of the coexisting limestone, but they are lower than those of the SD, which implies that D2 and D3 were altered by the fluids that buffered the SD. In addition, there is a general trend of gradually decreasing $\delta^{18}O$ with a corresponding increase in $^{87}Sr/^{86}Sr$ from D1 to D2, D3, and SD (Fig. 9C). The correlations between $\delta^{13}C$, $\delta^{18}O$, and $^{87}Sr/^{86}Sr$ reveal a two-end member trend, which consists of a seawater buffered member (D1 and calcite) and a hydrothermally buffered member (SD). Correspondingly, D2 and D3, which fall within the range of these two end members, experienced early dolomitization by seawater and then recrystallization by hydrothermal fluids during late diagenesis. The REE patterns of D2 and D3 differ from those of the limestone precursors (Fig. 11B), with slightly enriched HREEs and positive Eu anomalies (Fig. 11D), which further supports this interpretation.

5.3.4. Patchy dolostone (PD)

The PD is composed of subhedral dolomite with an obvious ring-band structure (Figs. 5H and 6H). Some bioclastic remnants are present in the PD (Fig. 5G), indicating that the dolomitization fluid replaced the bioclastic limestone. The PD has lower Mg/Ca (mol/mol) ratios (mean: 0.79) (Fig. 6B) and higher Sr concentrations (mean: 154.8 ppm) than the MD (Fig. 7D), indicating insufficient Mg in dolomitization fluid that formed PD. The low cation ordering (mean: 0.51) indicate that the dolomitization of PD is rapid (Gregg et al., 2015), which is consistent with rapid hydrothermal activity. Hydrothermal dolostones exhibit more negative $\delta^{18}O$ values than the host phases (Davies and Smith, 2006). The PD has the lowest $\delta^{18}O$ values (mean: −11.3‰) among the samples, which implies that the PD was formed by hydrothermal fluids. Furthermore, based on the homogenization temperatures of the inclusions of PD and the oxygen isotope thermometer for dolomite established by Horita (2014), the $\delta^{18}O_{VSMOW}$ of the dolomitization fluid of the PD ranged from +3‰ to + 6‰ (Fig. 14). The $\delta^{18}O_{VSMOW}$ values are significantly higher than those of Permian seawater (−2.2‰ to −1.0‰; Li et al., 2020a, b), which indicates a high temperature system (Spencer, 1987). The dolomitization fluid was most likely related to magmatic water ($\delta^{18}O_{VSMOW}$ value of generally + 4‰ to + 10‰; Hoefs, 2009), which was related to the regional basaltic eruption after the deposition of Maokou Formation in the southwestern Sichuan Basin (He et al., 2003). In addition, the $^{87}Sr/^{86}Sr$ ratios of the PD (0.7093–0.7102) are higher than those of the coeval seawater but are similar to those of the saddle dolomite which is precipitated from hydrothermal fluids (Fig. 9B). This suggests that the dolomitization fluid of the PD was most likely hydrothermal fluids resulting from the basaltic eruption in the southwestern Sichuan Basin. Finally, the total REE concentrations of the PD are higher than those of the coexisting limestone. In addition, the PAAS normalized REE patterns of the PD are HREE enriched with small positive Eu anomalies, which is similar to the REE patterns of the SD but is different from the REE patterns of the MD (Fig. 11C and D), further supporting the claim that the PD was formed from hydrothermal fluids.

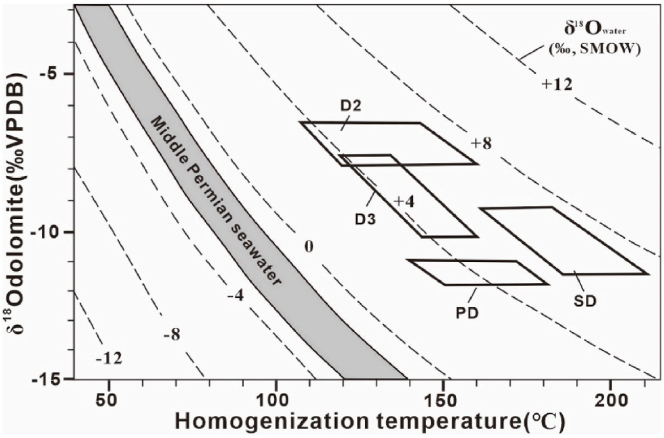

Fig. 14. Cross plots of $\delta^{18}O$ values (VPDB) versus homogenization temperature values of D2, D3, PD and SD. The $\delta^{18}O$water is following the Horita's (2014) equation.

5.4. Source of magnesium

The suitable source of Mg of dolomitization during burial setting has been widely discussed (Land, 1985; Wilson, 1990; Machel, 2004; Hollis et al., 2017). Mass balance calculations indicate that dolomitization of 1 m^3 of limestone requires 807 pore volumes of Mg-rich seawater (Land, 1985), therefore, it is difficult to form regional-scale dolomitization by basinal fluids in burial setting (Morrow, 1982; Land, 1985; Machel and Mountjoy, 1986; Machel, 2004). It has been proposed that MD has an isotopic signature that is suggestive of dolomitization from seawater in near-surface setting and then suffered an alteration by hydrothermal fluids. Whilst the LD and SD are hydrothermal in origin. Based on carbon isotope signatures, we suggest that the dolomitizing fluids is primarily composed of Permian seawater. Seawater is the volumetrically most viable source of magnesium (Wilson et al., 1990), especially when considering the volume of the MD in the Maokou Formation. However,

the lack of seawater-like REE profile, high $^{87}Sr/^{86}Sr$ ratios, high Fe concentrations, very high crystallization temperatures and fluid salinity of dolomite suggest that there is another hotter and deeper fluids. REE profile of PD and depletion of $\delta^{18}O$ suggests the fluids are possible related to basalts intrusions, and the olivine and clinopyroxene in the basalts can provide Mg and Fe to the dolomitizing fluids (Jacquemyn et al., 2014). The basalts are always more depleted in $\delta^{18}O$ than marine carbonates (Bindeman, 2008) and show obvious positive Eu anomalies and depleted HREEs (Douville et al., 2002), which is in consistent with the $\delta^{18}O$ and REE profile of PD. However, the $^{87}Sr/^{86}Sr$ ratios of the basalt are 0.7045–0.7065 (Shellnutt, 2014), which are much lower than the $^{87}Sr/^{86}Sr$ ratios of Permian seawater and the dolostone. The more radiogenic $^{87}Sr/^{86}Sr$ ratios of the dolostone are suggested to have resulted from the water-rock reaction between hydrothermal fluid and the underlying clastic strata (eg., Liangshan Fm) during the migration of hydrothermal fluid, which is also supported by the quartz cement precipitated in open vugs and pores. The study area is about 600 km away from the center of the basaltic eruption, thus the scale of hydrothermal emplacement may be small. Based on the mass balance, a volumetric ratio of at least 2.4 of basalt versus dolomite is required to provide an adequate amount of Mg, assuming 100% efficiency and complete leaching of basalt (Jacquemyn et al., 2014). Therefore, the Mg of hydrothermal fluids may provide enough Mg to form SD and LD, but not enough to explain the occurrence of MD. The temperture and salinities of the fluid inclusions of calcite cements that filled the vugs and intercrystal pores are similar to those of the surrounding dolomite (Fig. 10C), suggesting that the hydrothermal fluids were depleted in Mg resulting in incomplete alteration of the MD.

5.5. Influence of hydrothermal fluids on dolostone reservoir

Hydrothermal fluids contain some corrosive gases (SO_2, H_2S, and CO_2), which may lead to the dissolution on carbonate rocks (Davies, 2006; Bianca et al., 2016). The hydrothermal dolostone reservoirs in many sedimentary basins were generally developed along faults (Smith, 2006; Justine, 2006). However, there are also some failed wells, which were located along faults and aimed at hydrothermal reservoirs (Saller and Yaremko, 1994; Saller et al., 2001). This is due to the fact that minerals such as saddle dolomite, calcite, and quartz also precipitate and occlude porosity. Therefore, whether the hydrothermal fluids are beneficial to the formation of a reservoir depends on the amount of precipitation and dissolution. If the amount of precipitation is greater than the amount of dissolution, then it is destructive; otherwise, it is constructive. The hydrothermal fluids in the dolostone of Maokou Formation in the eastern Sichuan Basin were destructive for the following reasons. Based on the findings reported here, we conclude that D1 in the MD was not altered by hydrothermal fluids, while D2 and D3 in the MD were highly modified by hydrothermal fluids. However, intercrystalline porosity is often found associated with the D1 and the porosity of D1 is higher than those of D2 and D3 (Fig. 13A). The mean surface porosities of D1 in outcrop FNB and well TL6 are 3.5% and 3.1%, respectively, which are higher than those of D2 and D3 in FNB and TL6 (Fig. 13B). The mean Mg/Ca ratio of D1 (0.83) is lower than those of D2 (0.89) and D3 (0.92), indicating that Mg^{2+} was added to the dolomite and Ca^{2+} was removed during the hydrothermal alteration. However, calcite was observed in the intergranular pores and vugs of D2 and D3 under the microscope (Fig. 5D, F). In addition, the similar homogenization temperatures and salinities of the inclusions in the calcite and the surrounding dolomite (Fig. 10C) indicate that the calcite was precipitated in the nearby intercrystalline pores, fractures, and vugs of the dolostone, resulting in the deterioration of the reservoir's physical properties. Although there are some vugs in the dolostone of the Maokou Formation in the eastern Sichuan Basin, these vugs likely formed prior to the hydrothermal fluid migration, and were almost completely filled with saddle dolomite.

6. Conclusions

(1) In the eastern Sichuan Basin, the Middle Permian Maokou Formation carbonates were partly dolomitized after their deposition. Based on their petrographic textures, two types of matrix dolostone were identified: massive dolostone (MD) and patchy dolostone (PD). Based on the grain size of the dolomite, the MD was subdivided into three types: fine crystalline dolomite (D1), fine to middle crystalline dolomite (D2), and coarse crystalline dolomite (D3).

(2) The dolomitization fluid of the MD were derived from coeval seawater, and the MD was altered by hydrothermal fluids related to the regional basaltic eruption after formation. However, D1 in the MD was not altered, while D2 and D3 in the MD were highly altered.

(3) The PD, which is small in scale, is composed of coarse dolomite with a euhedral to subhedral texture, and it was formed by replacement resulting from hydrothermal fluids.

(4) The hydrothermal fluids in the dolostone of the Maokou Formation in the eastern Sichuan Basin were destructive in terms of the formation of a dolostone reservoir.

Declaration of competing interest

The authors declare that they have no known competing financial interests or personal relationships that could have appeared to influence the work reported in this paper.

Acknowledgements

This study was financially supported by the Strategic Priority Research Program of the Chinese Academy of Sciences (XDA14010306), NSFC Basic Research Program on Deep Petroleum Resource Accumulation and Key Engineering Technologies (U19B6003).

References

Adams, J.E., Rhodes, M.L., 1960. Dolomitization by seepage refluxion. AAPG Bull. 44, 1912–1920.
Al-Aasm, I., 2003. Origin and characterization of hydrothermal dolomite in the western Canada sedimentary basin. J. Geochem. Explor. 78–79, 9–15.
Al-Ramadan, K., Koeshidayatullah, A., Cantrell, D., Swart, P.K., 2019. Impact of basin architecture on diagenesis and dolomitization in a fault-bounded carbonate platform: outcrop analogue of a pre-salt carbonate reservoir, red sea rift, NM Saudi Arabia. Petrol. Geosci. 26 (3) https://doi.org/10.1144/petgeo2018–125.
Banner, J.L., Hanson, G.N., 1990. Calculation of simultaneous isotopic and trace element variations during water-rock interaction with applications to carbonate diagenesis. Geochem. Cosmochim. Acta 54, 3123–3137.
Banner, J.L., 1995. Application of the trace element and isotope geochemistry of strontium to studies of carbonate diagenesis. Sedimentology 42, 805–824.
Bau, M., Dulski, P., 1996. Distribution of yttrium and rare-earth elements in the penge and kuruman iron-formations, transvaal supergroup, South Africa. Precambrian Res. 79 (1–2), 0–55.
Bodnar, R., 1993. Revised equation and table for determining the freezing point depression of H2O-NaCl solutions. Geochem. Cosmochim. Acta 57, 683–684.
Budd, D.A., 1997. Cenozoic dolomites of carbonate islands: their attributes and origin. Earth Sci. Rev. 42, 1–47.
Chen, D.Z., Qing, H.R., Yang, C., 2004. Multistage hydrothermal dolomites in the middle devonian (givetian) carbonates from the guilin area, south China. Sedimentology 51, 1029–1051.
Chen, X., Zhao, W.Z., Zhang, L.P., Zhao, Z., Yang, Y., 2012. Discovery and exploration significance of structure-controlled hydrothermal dolomites in the Middle Permian of the central Sichuan Basin. Acta Pet. Sin. 33 (4), 562–569.
Davies, G.R., Boreen, T., Smith, L., 2005. Hydrothermal dolomite and leached limestone reservoirs: representative core fabrics and facies (abs. AAPG Annual Meeting Program 14, A32 (and extended abstract, CD format).
Davies, G.R., Smith, L.B., 2006. Structurally controlled hydrothermal dolomite reservoir facies: an overview. AAPG Bull. 90 (11), 1641–1690.
Douville, E., Charlou, J.L., Oelkers, E.H., Bienvenu, P., Colon, C.J., Donval, J.P., Fouquet, Y., Prieur, D., Appriou, P., 2002. The rainbow vent fluids (36 140 N, MAR): the influence of ultramafic rocks and phase separation on trace metal content in Mid-Atlantic Ridge hydrothermal fluids. Chem. Geol. 184, 37–48.
Gao, P., Li, S.J., He, Z.L., Wo, Y.J., Han, Y.Q., Li, X.C., 2020. Tectonic-sedimentary evolution of guangyuan-liangping paleo-rift in Sichuan Basin. Oil Gas Geol. 41 (4), 784–799 (in Chinese with English abstract).

Goldstein, R.H., 2001. Fluid inclusions in sedimentary and diagenetic systems. Lithos 55, 159–193.
Gregg, J.M., Sibley, D.F., 1984. Epigenetic dolomitization and the origin of xenotopic dolomite texture. J. Sediment. Petrol. 54, 908–931.
Gregg, J.M., Shelton, K.L., 1990. Dolomitization and dolomite neomorphism in the back reef facies of the Bonneterre and Davis formations (Cambrian), southeastern Missouri. J. Sediment. Petrol. 60, 549–562.
Guo, C., Chen, D., Qing, H., Dong, S., Li, G., Wang, D., 2016. Multiple dolomitization and later hydrothermal alteration on the upper Cambrian-lower Ordovician carbonates in the northern tarim basin, China. Mar. Petrol. Geol. 295–316.
Hardie, L.A., 1987. Dolomitization: a critical view of some current views. J. Sediment. Petrol. 57, 166–183.
He, B., Xu, Y.G., Xiao, L., Wang, K.M., Sha, S.L., 2003. Generation and sapatial distribution of the Eemeishan large igneous province: new evidence from stratigraphic records. Acta Geol. Sin. 77, 194–202 (in Chinese with English abstract).
He, B., Xu, Y.G., Wang, Y.M., Xiao, L., 2005. Nature of the Dongwu Movement and its temporal and spatial evolution. Earth Sci. 30 (1), 89–96 (in Chinese with English abstract).
He, B., 2016. Research progress on some issue on the Emeishan large igneous province. Adv. Earth Sci. 31, 23–42 (in Chinese with English abstract).
He, Y.B., Feng, Z.Z., 1996. Origin of fine to coarse grained dolostones of Lower Permian in Sichaun Basin and its peripheral regions. Journal of Jianghan Petroleum Istitute 18 (4), 15–20.
Hoefs, J., 2009. Stable Isotope Geochemistry, sixth ed. Springer-Verlag, Berlin.
Horita, J., 2014. Oxygen and carbon isotope fractionation in the system dolomite–water–CO2 to elevated temperatures. Geochem. Cosmochim. Acta 129, 111–124.
Hollis, C., Bastesen, E., Boyce, A., Corlett, H., Gawthorpe, R., Hirani, J., Rotevatn, A., Whitaker, F., 2017. Fault-controlled dolomitization in a rift basin. Geology 45 (3), 219–222.
Hu, A.P., Pan, L.Y., Hao, Y., Gu, M., 2018. Origin, characteristics and distribution of dolostone reservoir in qixia formation and MaoKou formation, Sichuan Basin, China [J]. Marine Origin Petroleum Geology 23 (2), 41–54 (in Chinese with English abstract).
Hu, M.Y., Hu, Z.G., Wei, G.Q., Yang, W., Liu, M.C., 2012. Sequence lithofacies paleogeography and reservoir prediction of the MaoKou formation in Sichuan Basin. Petrol. Explor. Dev. 39, 45–55.
Huang, S.J., Huang, K.K., Lv, J., 2014. The relationship between dolomite textures and their formation temperature: a case study from the Permian-Triassic of the Sichuan Basin and the Lower Paleozoic of the Tarim Basin. Petrol. Sci. 11 (1), 39–51.
Huang, H.Y., He, D.F., Li, Y.Q., Wang, B., 2017. The prototype and its evolution of the Sichuan sedimentary basin and adjacent areas during Liangshan and Qixia stages in Permian. Acta Petrol. Sin. 77, 1317–1337 (in Chinese with English abstract).
Jacquemyn, C., El Desouky, H., Hunt, D., Casini, G., Swennen, R., 2014. Dolomitization of the Latemar platform: fluid flow and dolomite evolution. Mar. Petrol. Geol. 55, 43–67.
Jones, B., 2005. Dolomite crystal architecture: genetic implications for the origin of the tertiary dolostones of the Cayman Islands. J. Sediment. Res. 75, 177–189.
Justine, A., Sagan, Bruce S., Hart, 2006. Three-dimensional seismic-based definition of fault-related porosity development: trenton–black river interval, saybrook, Ohio. AAPG (Am. Assoc. Pet. Geol.) Bull. 90 (11), 1763–1785.
Korte, C., Jasper, T., Heinz, W., Veizer, J., 2006. 87Sr/86Sr record of permian seawater. Palaeogeogr. Palaeoclimatol. Palaeoecol. 240, 89–107.
Land, L.S., 1980. The isotopic and trace element geochemistry of dolomite: the state of the art. In: Zenger, D.H., Dunham, J.B., Ethington, R.L. (Eds.), Concepts and Models of Dolomitization, vol. 28. SEPM Special Publication, pp. 87–110.
Land, L.S., 1985. The origin of massive dolomite. J. Geol. Educ. 33, 87–110.
Li, D., Chen, H., Liang, H., Peng, C., Duan, H., 2016. Relationship between reservoir development in the Middle Permian Maokou formation and paleostructure evolution in the sichuan basin. Oil Gas Geol. 37 (5), 756–763 (in Chinese with English abstract).
Li, P.P., Zou, H.Y., Hao, F., Yu, X.Y., Eiler, J.M., 2020a. Using clumped isotopes to determine the origin of the middle permian qixia formation dolostone, NW Sichuan Basin, China. Mar. Petrol. Geol. 122 (22), 104660.
Liu, J.Q., Zheng, H.F., Liu, B., Liu, H., Zhang, X., 2017. Characteristics and genetic mechanism of the dolomite in the middle permian MaoKou formation, central sichuan area. Acta Pet. Sin. 38 (4), 28–40.
Li, R., Hu, H., Shi, G.S., Cheng, W., 2020b. Genesis of dolomitization of permian MaoKou formation in langzhong area, northeastern Sichuan Basin. Xinjing Pet. Geol. 41 (2), 127–132.
Luczaj, J.A., Harrison, W.B., Smith Williams, N., 2015. Fractured hydrothermal dolomite reservoirs in the devonian dundee formation of the central Michigan basin. AAPG (Am. Assoc. Pet. Geol.) Bull. 90 (11), 1787–1801.
Lumsden, D.N., Chimahusky, J.S., 1980. Relationships between dolomite nonstoichiometry and carbonate facies parameters. In: Zenger, D.H., Dunham, J.B., Ethington, R.L. (Eds.), Concepts and Models of Dolomitization: Soc. Econ. Paleontologists Mineralogists. Spec. Pub. No. 28, pp. 123–137.
Machel, H., Lonnee, J., 2002. Hydrothermal dolomite—a product of poor definition and imagination. Sediment. Geol. 152 (3), 163–171.
Machel, H.G., 2004. Concepts and models of dolomitization: a critical reappraisal. In: Braithwaite, C.J.R., Rizzi, G., Darke, G. (Eds.), The Geometry and Petrogenesis of Dolomite Hydrocarbon Reservoirs, the Geological Society of London, vol. 235. Special Publication, pp. 7–63.
Ma, Y.S., Guo, X.S., Guo, T.L., Huang, R., Cai, X.Y., Li, G.X., 2007. The Puguang gas field-New giant discovery in the mature Sichuan Basin, SW China. AAPG (Am. Assoc. Pet. Geol.) Bull. 91, 627–643.
McLennan, S.M., 1989. Rare earth elements in sedimentary rocks: influence of provenance and sedimentary processes. In: Lipin, B.R., McKay, G.A. (Eds.), Geochemistry and Mineralogy of Rare Earth Elements 21. Mineralogical Society of America, United States, pp. 169–200.
Montañez, I.P., 1994. Late diagenetic dolomitization of Lower Ordovician, Upper Knox carbonates; a record of the hydrodynamic evolution of the southern Appalachian Basin. AAPG (Am. Assoc. Pet. Geol.) Bull. 78 (8), 1210–1239.
Morrow, D.W., 1982. Diagenesis 2. Dolomite: Part 2. Dolomitization models and ancient dolostones. Geosci. Can. 9, 95–107.
Qing, H., Mountjoy, E.W., 1994. Formation of coarsely crystalline, hydrothermal dolomite reservoirs in the Presqu'ile Barrier, Western Canada sedimentary basin. AAPG (Am. Assoc. Pet. Geol.) Bull. 78 (1), 55–77.
Qing, H.R., 1998. Petrography and geochemistry of early-stage, fine- and medium crystalline dolomites in the Middle Devonian Presqu'ile Barrier at Pine Point, Canada. Sedimentology 45, 433–446.
Saller, A.H., 2001. Reservoir characteristics of Devonian cherts and their control on oil recovery: dollarhide field, west Texas. AAPG (Am. Assoc. Pet. Geol.) Bull. 85 (1), 35–50.
Shellnutt, J.G., 2014. The Emeishan large igneous province: a synthesis. Geosci. Front. 5, 369–394.
Sibley, D.F., Gregg, J.M., 1987. Classification of dolomite rock textures. J. Sediment. Petrol. 57, 967–975.
Spencer, R.J., 1987. Origin of Ca–Cl brines in Devonian formations, Western Canada sedimentary basin. Appl. Geochem. 2, 373–384.
Sun, S.Q., 1994. A reappraisal of dolomite abundance and occurrence in the Phanerozoic: perspective. J. Sediment. Res. A64, 396–404.
Tucker, M.E., Wright, V.P., 1990. Carbonate Sedimentology. Blackwell Scientific Publication, Oxford.
Vahrenkamp, V.C., Swart, P.K., 1990. New distribution coefficient for the incorporation of strontium into dolomite and its implications for the formation of ancient dolomites. Geology 18 (5), 387–391.
Veizer, J., Ala, D., Azmy, K., Bruckschen, P., 1999. 87Sr/86Sr, δ13C and δ18O evolution of Phanerozoic seawater. Chem. Geol. 161, 59–88.
Warren, J., 2000. Dolomite: occurrence, evolution and economically important association. Earth Sci. Rev. 52, 1–81.
Wang, Y., Jin, Y., 2000. Permian palaeogeographic evolution of the jiangnan basin, south China. Palaeogeogr. Palaeoclimatol. Palaeoecol. 160, 35–44.
Wang, H., Shen, H., Huang, D., Shi, X.W., Yuan, X.L., Yang, Y.R., 2014. Origin and distribution of hydrothermal dolomites of the middle Permain in the Sichuan Basin. Nat. Gas. Ind. 34 (9), 25–32.
White, D.E., 1957. Thermal water of volcanic origin. Geol. Soc. Am. Bull. 68, 1637–1658.
Wilson, E.N., Hardie, L.A., Phillips, O.M., 1990. Dolomitization front geometry, fluid flow patterns, and the origin of massive dolomite: the Triassic Latemar buildup, northern Italy. Am. J. Sci. 290, 741–796.
Xiao, D., 2017. Research on Eogenetic Karst of Marine Carbonate and its Reservoir. Southwest Petroleum University (in Chinese with English abstract).
Yang, G., Wang, H., Shen, H., Yang, Y., Jia, S., Chen, W., 2015. Characteristics and exploration prospects of middle permian reservoirs in the Sichuan Basin. Nat. Gas. Ind. 35 (7), 10–16 (in Chinese with English abstract).
Zhai, G.M., 1989. Petroleum Geology of China, vol. 10. Petroleum Industry Press, Beijing (in Chinese).
Zhang, X.F., Cai, Z.X., Hu, W.X., Li, L., 2009. Using Adobe Photoshop to quantify rock textures. Acta Sedimentol. Sin. 27 (4), 667–673.
Zheng, H., Ma, Y., Chi, G., Qing, H., Liu, B., Zhang, X., Shen, Y., Liu, J., Wang, Y., 2019. Stratigraphic and structural control on hydrothermal dolomitization in the middle permian carbonates, southwestern Sichuan Basin (China). Minerals 9 (1), 1–31.
Zhu, C., Xu, M., Shan, J., Yuan, Y., Zhao, Y., Hu, S., 2009. Quantifying the denudations of major tectonic events in Sichuan basin:Constrained by the paleothermal records. Chin. Geol. 36, 1268–1277.
Zhu, C.Q., Xu, M., Yuan, Y.S., 2010. Palaeo-geothermal response and record of the effusing of Emeishan basalts in Sichuan basin. Chin. Sci. Bull. 55 (6), 474–482 (in Chinese with English abstract).
Zhou, J.G., Hao, Y., Deng, H.Y., Gu, M.F., Pan, L.Y., Yao, Q.Y., Yang, Y.R., Lou, X., 2019. Genesis and distribution of vuggy dolomite reservoirs of the lower permian qixia formation and MaoKou formation, western-central Sichuan Basin. Marine Origin Petroleum Geology 24 (4), 77–88 (in Chinese with English abstract).